ELSEVIER

Atom-based bond-order potentials for modelling mechanical properties of metals

M. Aoki [a], D. Nguyen-Manh [b], D.G. Pettifor [c], V. Vitek [d,*]

[a] *Department of Mathematical and Design Engineering, Faculty of Engineering, Gifu University, Yanagido, Gifu 501-1193, Japan*
[b] *EURATOM/UKAEA Fusion Association, Culham Science Centre, Abingdon OX14 3DB, UK*
[c] *Department of Materials, Oxford University, Parks Road, Oxford OX1 3PH, UK*
[d] *Department of Materials Science and Engineering, University of Pennsylvania, 3231 Walnut Street, Philadelphia, PA 19104, USA*

Abstract

Physical and mechanical properties of crystalline materials are commonly controlled by the atomic structure and atomic level behaviour of crystal defects. Both experimental observations and theoretical treatments of such complex atomic scale phenomena and structures are rather limited and it is the atomic level computer modelling that is the most promising approach in such research. The principal precursor of such calculations is a reliable description of atomic interactions. Rigorous density functional theory based calculations are limited either to ideal structures or to studies of periodic arrays of very closely spaced defects, owing to the application of periodic boundary conditions and feasible block sizes. Hence, studies of large and complex systems require approximations and simplifications when describing atomic interactions but these have to reflect correctly and with sufficient accuracy the physics of bonding. In transition metals and intermetallic compounds based on these metals the bonding has a mixed nearly-free electron and covalent character. This type of bonding is well described by bond-order potentials (BOPs) that are based on the chemically intuitive tight-binding approximation to the quantum mechanical electronic structure. Apart from the quantum mechanical character, another significant advantage of BOPs is that all the calculations can be performed in real space. In this paper we first review the theoretical background of BOPs and then present the procedure for fitting BOPs using both experimental data and results of DFT-based calculations. The parameters of BOPs that have been developed for titanium, molybdenum, iridium and Ti–Al alloys, together with testing of the transferability of these potentials, are summarised in

---

* Corresponding author. Tel.: +1 215 898 7883; fax: +1 215 573 2128.
   E-mail address: vitek@seas.upenn.edu (V. Vitek).

detail. In the final part we present the most representative applications of the BOPs to studies of dislocation cores and their effect on the dislocation glide. At this point we argue that these important features of the plastic behaviour relate directly to the angular character of bonding that is well represented by the BOPs.

Contents

1. Introduction

Many physical properties of crystalline materials, in particular their mechanical behaviour, are controlled by crystal defects, such as dislocations, stacking faults, grain boundaries and other interfaces, vacancies, interstitials, impurities and clusters of point defects. The atomic structure of such defects and their atomic level conduct often play a critical role and consequently knowledge of their structure and comprehension of their behaviour are crucial for fundamental understanding of properties of materials. While experimental techniques, such as high-resolution electron microscopy [1–4], are reaching resolution close to 1 Å, their capability to observe atomic level processes is fairly limited. At the same time theoretical treatment of such complex atomic scale phenomena and structures is very demanding and it is the atomic level computer modelling that is the most promising approach in such research (see papers and reviews in Refs. [5–10]).

The principal precursor of all atomic level studies, in particular those involving systems composed of a large number of atoms that do not form an ideal lattice, is a reliable

description of atomic interactions. The state-of-the-art first-principles methods based on the density functional theory (DFT), provide such a description most reliably [11–13]. However, these rigorous calculations are limited either to ideal structures without any defects or to studies of periodic arrays of very closely spaced defects, owing to the application of periodic boundary conditions and blocks of feasible sizes that contain at most a few hundred atoms. Studies of large and complex systems require approximations and simplifications when describing atomic interactions. The most common and successful approach is to coarse-grain the problem in that the electronic degrees of freedom are removed by imagining the atoms to be held together by some sort of glue or interatomic potential [14]. However, such potentials may obliterate some important features of bonding. For this reason, the most challenging aspect of materials modelling is the choice of the description of atomic interactions that correctly and with sufficient accuracy reflects the physics of bonding in any specific case, while at the same time it is computationally treatable for large systems of particles.

In the last two decades the most commonly used have been central-force many-body potentials [15], in particular the embedded-atom method [16–18] and Finnis–Sinclair potentials [19–21]. However, in transition metals and intermetallic compounds based on transition metals the bonding has a mixed nearly-free electron and covalent character. Indeed, it has been established a long time ago that it is the filling of the d-band that controls the cohesion and hence the particular ground state structure which a transition metal takes [22,23]. This bonding which is mediated by the d-electrons is covalent in character. This aspect of bonding is even more important in transition metal based intermetallic alloys, such as TiAl, where strong directional p–d bonds are formed between the sd-valent transition metals and sp-valent elements [24–27].

Various approximate schemes that include non-central forces have been advanced in recent years. They range from the empirical modified embedded-atom method [28–31] to the approach based on perturbation expansions employed in the framework of first-principles generalised pseudopotential theory [32–34]. In this paper, we summarise the recent developments of the many-atom Bond-Order Potentials (BOPs), which are based on the observation made by Coulson [35] in 1939 that the global description of energy bands with an associated band energy could be broken down into a local description of covalent bonds with associated individual bond energies. As described in the preceding paper by Finnis, they give an exact representation of the bond energy within the chemically intuitive tight-binding (TB) approximation to the quantum mechanical electronic structure [36–41] and retain thus the angular character of bonding. This method, using an orthogonal TB basis and two-centre bond integrals has been implemented in the Oxford order-N package (OXON) [42–45]. Apart from the quantum mechanical character, another significant advantage of BOPs is that modelling of extended defects, which requires a large number of atoms, can be performed in real space. This broadens the range of solvable problems and avoids using periodic boundary conditions necessary in k-space methods. Within the BOPs scheme, the Hellmann–Feynman theorem [46,47] can be used to evaluate forces on the atoms and the computational effort scales linearly with the number of atoms in the system, decreasing thus dramatically the computational time.

The BOPs have now been developed for titanium [48], molybdenum [49], iridium [50,51] and Ti–Al alloys [52] and they are being developed for molybdenum silicides [53], tungsten and other bcc transition metals. Details of their construction and testing are presented in Section 4 and their application in studies of dislocation properties are summarised in

Section 5 of this paper. In Section 2 and Appendices A and B we review the theoretical background of BOPs. The procedure for fitting BOPs using both experimental data and results of DFT-based calculations, which includes implementation of the analytical screened bond integrals, is presented in Section 3.

2. The covalent bond energy

2.1. On-site representation

The bcc transition metal, W, has the highest cohesive energy of all the elements in the periodic table. This reflects the fact that the bonding in transition metals is not that of the classic metallic bond of sp-valent metals such as Al, where the ion cores are immersed in the free electron gas formed from the delocalisation of the valence electrons. Instead the bonding in transition metals is driven by the interaction between the localised valence d-electrons, giving rise to unsaturated covalent bonds, which are well-approximated by the orthogonal tight-binding (TB) model. Even though these bonds are unsaturated rather than saturated, there is no corresponding promotion energy penalty to pay as in C and Si where the formation of sp^3 hybrids costs about 7 eV/atom. Thus, W has a cohesive energy of 8.9 eV/atom compared to the 7.4 and 4.6 eV/atom for C and Si.

The binding energy, E^{B}, of non-magnetic transition metals may, therefore, be approximated by the sum of repulsive and attractive contributions, namely

$$E^{\mathrm{B}} = E^{\mathrm{rep}} + E^{\mathrm{cov}} \tag{1}$$

where the promotion, ionic, and magnetic energies in Eq. (69) of [54] may be neglected. In our treatment of transition metals and intermetallics the repulsive energy is further broken down into two contributions

$$E^{\mathrm{rep}} = E^{\mathrm{pair}} + E^{\mathrm{core}} \tag{2}$$

E^{pair} is the usual pairwise contribution arising from the overlap repulsion, whereas E^{core} originates from the strong repulsion which the valence sp-electrons experience in transition metals and their alloys. These will be discussed in detail in Section 3.

The covalent bond energy is evaluated within the orthogonal TB approximation, so that

$$E^{\mathrm{cov}} = \sum_{I\mu} 2 \int^{\varepsilon_{\mathrm{F}}} (\varepsilon - \varepsilon_{I\mu}) D_{I\mu}(\varepsilon) \, \mathrm{d}\varepsilon \tag{3}$$

where the local density of states associated with the orbital μ on atomic site I is given by the imaginary part of the diagonal Green's function matrix element (c.f. Eqs. (37) and (73) of [54])

$$D_{I\mu}(\varepsilon) = -\frac{1}{\pi} \lim_{\eta \to 0} \mathrm{Im} \, G^{I\mu, I\mu}(\varepsilon + \mathrm{i}\eta) \tag{4}$$

$\varepsilon_{I\mu}$ is the on-site atomic energy level of orbital μ on site I, corresponding to ε_{Id} for the d orbitals on transition metal sites and ε_{Ip} for the p orbitals on Al sites in TiAl, the intermetallic considered in this paper. ε_F is the Fermi energy and the prefactor 2 before the integral sign accounts for the spin degeneracy of our non-magnetic systems. The relative positions of the on-site energies $\varepsilon_{I\mu}$ are adjusted self-consistently to guarantee local charge neutrality (LCN), which is an excellent approximation for metals [23].

The dependence of the shape of the electronic densities of states $D_{I\mu}(\varepsilon)$ on the local atomic environment surrounding atom I may be made by coarse-graining $D_{I\mu}(\varepsilon)$ in terms of its moments μ_p using the Lanczos recursion method [55], as discussed in §7.1 of [12]. The diagonal matrix element of the Green's function $G^{I\mu,I\mu}(\varepsilon)$ in Eq. (4) may then be expanded as the continued fraction (relabelling the atomic state $|I\mu\rangle$ by $|0\rangle$)

$$G_{00}(\varepsilon) = \cfrac{1}{\varepsilon - a_0 - \cfrac{b_1^2}{\varepsilon - a_1 - \cfrac{b_2^2}{\varepsilon - a_2 - \cfrac{b_3^2}{\varepsilon - \cdots}}}} \tag{5}$$

where the Lanczos recursion coefficients are related to the moments μ_p of the density of states through

$$\begin{aligned}
\mu_1 &= a_0 \\
\mu_2 &= a_0^2 + b_1^2 \\
\mu_3 &= a_0^3 + 2a_0 b_1^2 + a_1 b_1^2 \\
\mu_4 &= a_0^4 + 3a_0^2 b_1^2 + 2a_0 a_1 b_1^2 + a_1^2 b_1^2 + b_1^4 + b_1^2 b_2^2
\end{aligned} \tag{6}$$

etc. The pth moment can be computed by summing over all self-returning bonding/hopping paths of length p since from Eq. (75) of [54] we have

$$\mu_p = \langle 0|\widehat{H}^p|0\rangle \tag{7}$$

For bulk metallic systems the continued fraction needs to be terminated at some level depending on the required accuracy. It is customary to approximate the continued fraction at some level L by setting the coefficients as constants for $n \geqslant L$ by continuing $a_n = a_\infty$ and $b_n = b_\infty$. This approximation defines the so-called square root terminator

$$T(\varepsilon) = \frac{b_\infty^2}{\varepsilon - a_\infty - T(\varepsilon)} = \frac{1}{2}\left[\varepsilon - a_\infty - \sqrt{\varepsilon - a_\infty - 2b_\infty}\sqrt{\varepsilon - a_\infty + 2b_\infty}\right] \tag{8}$$

Thus, the continued fraction in Eq. (5) is terminated at level L with

$$\varepsilon - a_{L-1} - T(\varepsilon) \tag{9}$$

It is clear from the behaviour of the square root term in Eq. (8) that a continuous band of electronic states now runs from $\varepsilon = a_\infty - 2b_\infty$ through to $\varepsilon = a_\infty + 2b_\infty$. A useful prescription is given in [56] for choosing the a_∞ and b_∞, which determine the resultant band centre a_∞ and bandwidth $4b_\infty$.

As an example of the power of the recursion method consider the relative stabilities of the fcc, bcc, and hcp lattices across the transition metal series. Neglecting the magnetic 3d elements, the non-magnetic 3d, 4d and 5d transition metals display the well-known trend from hcp to bcc to hcp to fcc as the valence shell fills with d-electrons. Using canonical TB hopping parameters in which ddσ:ddπ:ddδ = −6:4:−1, the recursion coefficients a_n, b_n may be calculated, as given in Table 1. The energy reference has been taken with respect to the on-site atomic energy level, so that from Eqs. (6) and (7) $a_0 \equiv \mu_1 = \langle 0|\widehat{H}|0\rangle = 0$. We see that the values of $b_1^2 \equiv \mu_2 = \langle 0|\widehat{H}^2|0\rangle$, which determine the mean square width of the band, are almost identical for all three lattices. In addition, the fcc and hcp bands are

Table 1
Averaged canonical d-band recursion coefficients normalized by $|dd\sigma|$ for the first nearest neighbours

	bcc	fcc	hcp
a_0	0.0000	0.0000	0.0000
b_1	1.9144	2.1602	2.1602
a_1	−0.4447	−0.5181	−0.5181
b_2	1.5178	1.8949	1.8889
a_2	−0.1456	−0.7845	−0.7972

skewed by the same amount since their values of $a_1 = \mu_3/\mu_2$ are identical, with bcc being only slightly less skewed.

The first significant difference in the recursion coefficients between the three lattices occurs at b_2 which depends on the fourth moment μ_4 as

$$(b_2/b_1)^2 = \mu_4/\mu_2^2 - \mu_3^2/\mu_2^3 - 1 \qquad (10)$$

We see from the continued fraction Eq. (5) that when b_2 vanishes, then the spectrum will be purely bimodal, so that b_2 is a measure of the uni- versus bimodal behaviour of the density of states. It is clear from Table 1 that the bcc density of states is more bimodal than fcc and hcp. Finally, as expected, the fcc and hcp density of states will be very similar since they have almost identical first four moments μ_1, μ_2, μ_3 and μ_4.

Fig. 1 compares the bond energies of bcc (solid curves) and hcp (dashed curves) with those of fcc as a function of d-band filling for three different levels of approximation: $M = 4$, 6 and 18 corresponding to including up to the 4th, 6th and 18th moments exactly in the continued fraction, Eq. (5). We see that the fourth moment is sufficient to stabilise the bcc structure in the middle of the series and to destabilise it towards the band edges. This is consistent with the bcc density of states being more bimodal than fcc and hcp, since it takes a smaller value of b_2 in Table 1. On the other hand, we require the sixth moment to differentiate between the close-packed structures fcc and hcp. Thus, including up to μ_6 in the continued fraction (by summing over all self-returning hopping paths up to the length
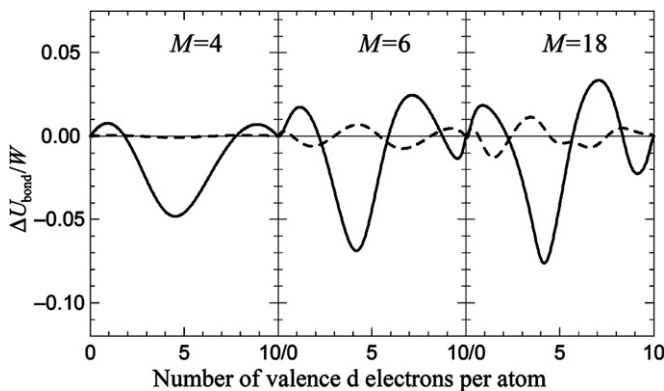
Fig. 1. The difference in the bond energies, normalised by the band width W, of bcc (solid curves) and hcp (dashed curves) compared to that of fcc as a function of d-band filling for three different levels of termination of continued fraction (Eq. (5)) retaining exact moments up to μ_M. The canonical d-band model has been used for the bond integrals, i.e. $(dd\sigma, dd\pi, dd\delta) = (-6, 4, -1)(2W/5)(s/r)^5$ with an equal Wigner–Seitz sphere radius s for all structures.

six about the atom) is sufficient to predict the structural trend from hcp to bcc to hcp to fcc as observed experimentally across the transition metal series. Only the fcc phase of Ni, Pd and Pt is not predicted due to the neglect of sd hybridisation, which becomes increasingly important as the d-band fills.

Thus, the recursion technique provides a rapidly convergent order N method for obtaining the covalent bond energies in transition metals and intermetallics using the *on-site representation* of Eq. (3). Unfortunately, however, for modelling their mechanical properties we need not only the energy but also the forces in order to relax the dislocation core structures, for example. This requires going beyond the on-site representation to the less well converged inter-site representation, which we now discuss.

2.2. Inter-site representation

The covalent bond energy associated with atom I may be decomposed in terms of the contributions from the individual bonds IJ. It follows from Eqn. (65) of [54] that

$$E^{\mathrm{cov}} = \frac{1}{2} \sum_{I \neq J} E^{\mathrm{cov}}_{IJ} \tag{11}$$

where

$$E^{\mathrm{cov}}_{IJ} = 2 \sum_{\mu, v} H_{I\mu, Jv} \Theta_{Jv, I\mu} \tag{12}$$

with

$$\Theta_{I\mu, Jv} = -\frac{2}{\pi} \int^{\varepsilon_F} \lim_{\eta \to 0} \mathrm{Im}\, G_{I\mu, Jv}(\varepsilon + \mathrm{i}\eta)\, \mathrm{d}\varepsilon \tag{13}$$

$H_{I\mu, Jv}$ are the matrix elements of the two-centre TB Hamiltonian which may be written in terms of the usual Slater–Koster two-centre bond integrals and direction cosines [57]. $\Theta_{I\mu, Jv}$ are the matrix elements of the bond order, which may be expressed in terms of an integral over the corresponding inter-site Green's function as in Eq. (13).

The term 'bond order' was introduced by the chemists because the bond order is one-half the difference between the number of electrons in the bonding state compared to the antibonding state. Defining the bonding $|+\rangle$ and antibonding $|-\rangle$ states by

$$|\pm\rangle = (|I\mu\rangle \pm |Jv\rangle)/\sqrt{2} \tag{14}$$

then

$$G_{I\mu, Jv} = \frac{1}{2}(G_{++} - G_{--}) \tag{15}$$

where $G_{++} = \langle + | \widehat{G} | + \rangle$ and $G_{--} = \langle - | \widehat{G} | - \rangle$. Therefore, substituting Eq. (15) into Eq. (13) we have

$$\Theta_{I\mu, Jv} = \frac{1}{2}(N_+ - N_-) \tag{16}$$

where $N_{+(-)}$ gives the number of electrons in the bonding (antibonding) state. The bond order is more commonly known to physicists as the density matrix since $\Theta_{I\mu, Jv} = 2\rho_{I\mu, Jv}$ from Eq. (13).

Thus, within the inter-site representation the covalent bond energy is written as the sum over individual bond contributions, which take the chemically intuitive form as the

product of bond integrals and bond orders. The inter-site representation Eq. (12) follows directly from the on-site representation Eq. (3), since the Green's function satisfies the matrix equation

$$(\mathbf{H} - \varepsilon\mathbf{I})\mathbf{G} = -\mathbf{I} \tag{17}$$

The inter-site representation allows an immediate derivation of the Hellmann–Feynman force on an atom K [46,47], namely

$$\mathbf{F}_K^{\text{cov}} = -\sum_{I \neq J} \sum_{\mu,\nu} (\nabla_K H_{I\mu,J\nu})\Theta_{J\nu,I\mu} \tag{18}$$

This follows from Eq. (12) since the corresponding contribution involving the first order change in bond order or density matrix vanishes by first order perturbation theory.

The expansion (18) for the force appears deceptively simple, since once we have evaluated the bond order (which we need for the energy) then the force is given 'free' as the gradients of the Slater–Koster Hamiltonian that is trivial to evaluate. Unfortunately, the off-diagonal Green's functions required for the bond orders are very poorly converged if they are computed using the recursion method as the difference of two diagonal Green's functions G_{++} and G_{--}, as in Eq. (15) [58]. This led to the development of an alternative procedure for evaluating $G_{I\mu,J\nu}$ which we discuss in the next section.

2.3. Atom-based exact many-atom expansion for the bond order

A stable, convergent method for evaluating the inter-site Green's functions for metals was developed during late 80s and early 90s by Aoki and Pettifor [36,39,41,59]. For simplicity let us consider the case of a single orbital $|I\rangle$ on each atomic site. Rather than starting with a Lanczos orbital centred on a given site I, which is natural for evaluating the diagonal on-site Green's function $G_{I,I}$ as in Section 2.1, they took a starting Lanczos orbital $|u_0^\lambda\rangle$ that was an admixture of orbitals on sites I and J, namely

$$|u_0^\lambda\rangle = c_I|I\rangle + c_J e^{i\phi}|J\rangle \tag{19}$$

where $\lambda = \cos\phi$ and $c_I^2 + c_J^2 = 1$. Then

$$G_{00}^\lambda = \langle u_0^\lambda|(\varepsilon - \widehat{H})^{-1}|u_0^\lambda\rangle = c_I^2 G_{I,I} + c_J^2 G_{J,J} + 2c_I c_J \lambda G_{I,J} \tag{20}$$

Hence, we can write the *inter-site* Green's function $G_{I,J}$ as the derivative of the *diagonal* Green's function G_{00}^λ, namely

$$G_{I,J} = \frac{1}{2c_I c_J}\frac{\mathrm{d}G_{00}^\lambda}{\mathrm{d}\lambda} \tag{21}$$

That is the inter-site Green's function tells us how the information is passed back and forward between I and J as the phase of the bond orbital $|u_0^\lambda\rangle$ is changed.

But the diagonal Green's function G_{00}^λ can be written as a continued fraction in terms of the recursion coefficients $\{a_n^\lambda, b_n^\lambda\}$ as in Eq. (5). Thus using the chain rule we can write

$$\frac{\mathrm{d}G_{00}^\lambda(\{a_n^\lambda, b_n^\lambda\})}{\mathrm{d}\lambda} = \sum_{n=0}^\infty \frac{\partial G_{00}^\lambda}{\partial a_n^\lambda}\frac{\partial a_n^\lambda}{\partial \lambda} + \sum_{n=1}^\infty \frac{\partial G_{00}^\lambda}{\partial b_n^\lambda}\frac{\partial b_n^\lambda}{\partial \lambda} \tag{22}$$

The derivatives of G_{00}^λ with respect to the recursion coefficients are given by Dyson's equation [60]

$$\frac{\partial G_{00}^\lambda}{\partial a_n^\lambda} = G_{0n}^\lambda G_{n0}^\lambda \tag{23}$$

and

$$\frac{\partial G_{00}^\lambda}{\partial b_n^\lambda} = 2G_{0(n-1)}^\lambda G_{n0}^\lambda \tag{24}$$

where the G_{0n}^λ are the Green's functions defined along the semi-infinite Lanczos chain (see Fig. 1 of [54]). The derivatives of the recursion coefficients with respect to the phase λ are given by

$$\frac{\partial a_n^\lambda}{\partial \lambda} = \sum_{r=1}^{2n+1} \frac{\partial a_n^\lambda}{\partial \mu_r^\lambda} \frac{\partial \mu_r^\lambda}{\partial \lambda} = 2c_I c_J \sum_{r=1}^{2n+1} \frac{\partial a_n^\lambda}{\partial \mu_r^\lambda} \zeta_{r+1}^{IJ} \tag{25}$$

$$\frac{\partial b_n^\lambda}{\partial \lambda} = \sum_{r=1}^{2n} \frac{\partial b_n^\lambda}{\partial \mu_r^\lambda} \frac{\partial \mu_r^\lambda}{\partial \lambda} = 2c_I c_J \sum_{r=1}^{2n} \frac{\partial b_n^\lambda}{\partial \mu_r^\lambda} \zeta_{r+1}^{IJ} \tag{26}$$

because

$$\mu_p^\lambda = \langle u_0^\lambda | \widehat{H}^p | u_0^\lambda \rangle = c_I^2 \mu_p^I + c_J^2 \mu_p^J + 2c_I c_J \lambda \zeta_{p+1}^{IJ} \tag{27}$$

where ζ_{r+1}^{IJ} is the interference path linking atoms I and J via r-hops, that is

$$\zeta_{r+1}^{IJ} = \langle I | \widehat{H}^r | J \rangle \tag{28}$$

Hence, substituting Eqs. (22)–(28) into Eq. (21) and taking $\lambda = 0$ we have derived the following exact many-atom expansion for the bond order

$$\Theta_{IJ} = 2 \left[\sum_{n=0}^{\infty} \chi_{0n,n0} \delta a_n^{IJ} + 2 \sum_{n=1}^{\infty} \chi_{0n,(n-1)0} \delta b_n^{IJ} \right] \tag{29}$$

where the response functions are defined by

$$\chi_{0m,n0} = \lim_{\eta \to 0} \frac{1}{\pi} \text{Im} \int^{\varepsilon_F} G_{0m}(\varepsilon + i\eta) G_{n0}(\varepsilon + i\eta) \, d\varepsilon \tag{30}$$

The first few δa_n and δb_n are given by

$$\delta a_0^{IJ} = \zeta_2^{IJ}, \quad \delta b_1^{IJ} = (1/2\mu_2^{1/2})\zeta_3^{IJ} \quad \text{and} \quad \delta a_1^{IJ} = (1/\mu_2)\zeta_4^{IJ} - (\mu_3/\mu_2^2)\zeta_3^{IJ} - 2\zeta_2^{IJ} \tag{31}$$

where

$$\mu_p = \mu_p^{\lambda=0} = c_I^2 \mu_p^I + c_J^2 \mu_p^J \tag{32}$$

Thus, the bond order has been written as a *linear* function of the interference paths linking I and J but with prefactors that depend *non-linearly* on the moments.

Transition metals and intermetallics are characterised by unsaturated covalent bonds unlike the case of semiconductors with their saturated σ bonds. This difference in behaviour is captured by the many-atom expansion by taking different values for c_I and c_J for
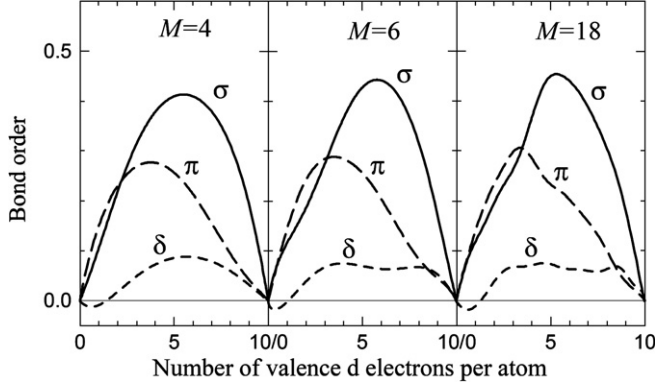
Fig. 2. The σ, π and δ bond orders in d bonded fcc structure, evaluated using the atom-based bond order expansion, Eq. (29), for three different levels of termination of continued fraction (Eq. (5)) retaining exact moments up to μ_M. Truncators described in Appendix B are used.

metals as compared to semiconductors. For metals most rapid convergence of the expansion is obtained by the *atom-based* representation, in which we take

$$c_I \to 1, \quad c_J \to 0 \tag{33}$$

so that the moments which enter the bond order expansion through Eq. (32) are given by

$$\mu_p = \mu_p^I \tag{34}$$

On the other hand, for semiconductors most rapid convergence is obtained by the *bond-based* representation, in which we take

$$c_I = c_J = 1/\sqrt{2} \tag{35}$$

so that the moments are given by

$$\mu_p = \frac{1}{2}(\mu_p^I + \mu_p^J) \tag{36}$$

This bond-based representation is discussed in the following paper [61].

Aoki [39] has generalised this atom-based representation to the case of multi-orbital atoms when the moments μ_p^I are the average d and p moments about site I (see Appendix A). This allowed the appropriate termination of the many-atom expansion (see Appendix B) that satisfies the equivalence of the on-site and inter-site expressions for the covalent bond energy [39,42,45], which guarantees the inter-site scheme to give the same convergence as the on-site scheme. Fig. 2 demonstrates the good convergence that is obtained for the bond order within this atom-based approach.

An alternative atom-based scheme has recently been proposed by Ozaki [62], in which the inter-site Green's functions are expanded using the basis vectors of the block Lanczos algorithm. (See [63] for the formalism and comparison with other methods.)

3. Procedure for fitting bond-order potentials

The important aspect of the fitting scheme is that the three parts of the bonding energy, E^{cov}, E^{core} and E^{pair} are developed independently and sequentially. First, E^{cov} is constructed

based solely on *ab initio* data with no empirical input. However, the numbers of valence electrons in the bands included in the evaluation of E^{cov} may require empirical adjustment relative to those found in ab initio calculations. Next E^{core} is fitted to reproduce the Cauchy pressures, ($C_{12} - C_{44}$ for the case of cubic symmetry; $C_{12} - C_{66}$ and $C_{13} - C_{44}$ for hexagonal and tetragonal symmetries). Finally, the pair potential, determining E^{pair}, is fitted to reproduce the lattice parameters, remaining elastic moduli and cohesive energy.

The most important quantities entering E^{cov}, which is given by Eqs. (11)–(13), are the two-centre bond integrals, β_τ, where $\tau = \sigma$, π or δ and β corresponds to various combinations of orbital quantum numbers, such as dd, dp, pp etc. The angular dependence of the inter-site Hamiltonian matrix elements takes the usual Slater and Koster form [57]. For a given Hamiltonian the bond order is determined as described in Section 2. In practical calculations it is evaluated using the Oxford order-N (OXON) package. For metals a fictitious temperature is also introduced into the formalism in order to damp down the long-range Friedel oscillations, thereby guaranteeing the convergence of the bond order and hence the Hellmann–Feynman forces, which are needed for atomistic simulations. Details of implementations of the theory summarised in Section 2 together with introduction of the fictitious temperature can be found in [42,43]. In all the fittings described below we have found that sufficient accuracy is provided by $k_{\text{B}}T_{\text{e}} = 0.3$ eV if BOP theory retains contributions up to the ninth moment in the local electronic density of states. The individual forces on all the atoms in our calculations are then converged to better than 0.01 eV Å^{-1}.

The dependence of the bond integrals on the distance between the atoms I and J, r_{IJ}, needs to be represented by a continuous differentiable function and for this purpose we have employed the generalised Goodwin–Skinner–Pettifor (GSP) form [64]

$$\beta_\tau(r_{IJ}) = \beta_\tau(r_0)\left(\frac{r_{IJ}}{r_0}\right)^{n_a} \exp\left\{n_b\left[\left(\frac{r_0}{r_c}\right)^{n_c} - \left(\frac{r_{IJ}}{r_c}\right)^{n_c}\right]\right\} \tag{37}$$

where r_0 is the equilibrium first nearest neighbours separation; n_a, n_b, n_c and r_c are for a given β and τ fitting parameters. These are fitted such as to reproduce results of first-principles TB-LMTO calculations (for more details see [65]). However, in non-close-packed structures, such as bcc, there is a marked discontinuity between the distance dependencies of the first and second shells and thus the data cannot be fitted directly by the GSP form. This phenomenon is the result of the screening of the bond integrals by the local environment. It was first captured by the empirical environment dependent tight-binding (EDTB) scheme [66] and we represent this environment dependence of the screened bond integrals $\tilde{\beta}_\tau^{IJ}$ through the analytic expression derived from non-orthogonal TB [65,67], namely

$$\tilde{\beta}_\tau^{IJ} = \beta_\tau(r_{IJ})(1 - S_\tau^{IJ}) \tag{38}$$

The unscreened bond integrals $\beta_\tau(r_{IJ})$ are pairwise functions and are well represented by the GSP form. The screening function S_τ^{IJ}, which results from the screening of the $I - J$ d–d bond by the s-valence orbitals on the neighbouring atoms K [67], takes the form [49]

$$S_\tau^{IJ} = \frac{c_{1\tau}^{IJ} - \bar{\mu}_{2\tau}}{1 + O_\tau^2(r_{IJ}) - 2\bar{\mu}_{2\tau}} \tag{39}$$

where $O_\tau(r_{IJ})$ is the d–d overlap integral between orbitals centred on atoms I and J. $c_{1\tau}^{IJ}$ is the interference contribution that results from the electrons hopping between the σ, π or δ valence d orbitals on atoms I and J via the surrounding lattice. The dominant contribution

is the two-hopping path from $I \rightarrow K \rightarrow J$ via an unscreened bond integral $\beta_{ds\sigma}$ and overlap integral $O_{ds\sigma}$. A much smaller contribution results from three-hops from $I \rightarrow K \rightarrow I \rightarrow J$. Higher terms are negligible. The expression for $c_{1\tau}^{IJ}$ can be summed up as [49]

$$c_{1\tau}^{IJ} = A_\tau \sum_{k \neq i,j} [(1 + \delta_{\tau 0})/4][1/\beta_\tau(r_{IJ})] \{ [\beta_{ds\sigma}(r_{IK}) O_{sd\sigma}(r_{KJ}) + O_{ds\sigma}(r_{IK}) \beta_{sd\sigma}(r_{KJ})]$$
$$\times g_\tau(\Theta_{JIK}) g_\tau(-\Theta_{IJK}) - [\beta_{ds\sigma}(r_{IK}) O_{sd\sigma}(r_{KI}) O_\tau(r_{IJ}) g_\tau^2(\Theta_{JIK})$$
$$+ O_\tau(r_{IJ}) O_{ds\sigma}(r_{KJ}) \beta_{sd\sigma}(r_{JK}) g_\tau^2(\Theta_{IJK})] \} \tag{40}$$

where $\delta_{\tau 0}$ equals 1 for $\tau = \sigma$ but 0 for $\tau = \pi$ or δ. A_τ equals 1 in [67] but it can be used as a fitting parameter. The s–d bond integral $\beta_{ds\sigma}$ takes the GSP form. We have assumed that the overlap integrals fall off with distance in the same way as the corresponding bond integrals, so that each overlap integral introduces a single new fitting parameter $O(r_0)/\beta(r_0)$. As might be expected, the interference contributions are dependent on the angular character of the d-bond that is being screened through the angular functions

$$g_\sigma(\theta) = (1/4)(1 + 3\cos 2\theta)$$
$$g_\pi(\theta) = (\sqrt{3}/2)\sin 2\theta \tag{41}$$
$$g_\delta(\theta) = (\sqrt{3}/4)(1 - \cos 2\theta)$$

The screening function S_τ^{IJ} in Eq. (39) is further weakly renormalised through the presence of the two-hop second moment contribution $\bar{\mu}_{2\tau} = \frac{1}{2}(\mu_{2\tau}^I + \mu_{2\tau}^J)$, where

$$\mu_{2\tau}^I = O_\tau^2(r_{IJ}) + A_\tau \sum_{K \neq I} [(1 + \delta_{\tau 0})/2] O_{ds\sigma}^2 g_\tau^2(\Theta_{JIK}) \tag{42}$$

Since separation of atoms I and J may come very close to the interaction cut-off during the relaxation calculation, S_τ^{IJ} could in this case become larger than one. In order to avoid such unphysical value S_τ^{IJ} is always cut-off such that its value cannot exceed one.

The 'core' contribution, E^{core}, represents the repulsion due to the valence s- and p-electrons being squeezed into the ion core regions under the influence of the large covalent d-bonding forces in transition metals and intermetallics. It is described by a screened Yukawa-type potential [65,68]:

$$E^{core} = \frac{1}{2} \sum_I \sum_{J \neq I} \frac{\sqrt{B^{s_I} B^{s_J}}}{r_{IJ}} \exp\left[-\frac{1}{2} \lambda^{s_I s_J} \left(r_{IJ} - \left(r_{core}^{s_I} + r_{core}^{s_J} \right) \right) \right] \tag{43}$$

where s_I and s_J label species at positions I and J that are, in general different in alloys. $r_{core}^{s_I}$ is the core radius and $\lambda^{s_I s_J} = \frac{1}{2}(\lambda^{s_I} + \lambda^{s_J})$ is the screening exponent that is dependent on the local density and environment of atoms I and J. We model the environmental dependence through an embedded-atom-type expression by writing:

$$\lambda^{s_I} = \lambda_0^{s_I} + \left[\sum_{K \neq I} C^{s_I} \exp(-v^{s_I} r_{IK}) \right]^{\frac{1}{m^{s_I}}} \tag{44}$$

where $\lambda_0^{s_I}$ (the unscreened value of the exponent), C^{s_I}, v^{s_I} and m^{s_I} are all adjustable parameters that are different for different chemical species.

The contribution to the binding energy, E^{pair}, arises nominally from the overlap repulsion and the electrostatic interaction between the atoms. It can be expressed as

$$E^{\text{pair}} = \frac{1}{2} \sum_{I \neq J} V(r_{IJ}) \tag{45}$$

where $V(r_{IJ})$ is a pair potential. For this pair potential we employ the same functional form as that used in [20] when constructing Finnis–Sinclair potentials, namely a sum of cubic splines:

$$V(r_{IJ}) = \sum_k A_k (r_k - r_{IJ})^3 H(r_k - r_{IJ}) \tag{46}$$

with $H(x)$ the Heaviside step function. The node points r_k and coefficients A_k are used as fitting parameters. The functional form of the pair potential assures that $V(r_{IJ})$, as well as its first and second derivatives, are everywhere continuous and equal to zero at the cut-off distance r_1.

Since the reason for the development of any empirical potential is its use in computer modelling of crystal defects, in particular extended defects such as interfaces and dislocations, some unphysical structural instabilities or metastable configurations must not occur in the cores of such defects when using this potential. Whilst this can never be guaranteed absolutely, it is essential to carry out sufficiently convincing tests that such circumstances are unlikely to arise. Such tests are an integral part of the development of potentials and are briefly described in the following section summarising the BOPs constructed for specific materials.

4. Bond-order potentials for transition metals and intermetallic compounds

4.1. HCP titanium [48]

In constructing the BOP for hexagonal-close-packed titanium only d-electrons were included explicitly in E^{cov} since their covalent character determines the stability of this crystal structure [23,69]. Hence, the only bond integrals needed are ddσ, ddπ and ddδ. These were assumed to display a power law dependence on distance, which in the framework of Eq. (37) means $\beta = \text{dd}$, $\tau = \sigma, \pi, \delta$ and $n_b = 0$. r_0 is taken as the nearest neighbour distance in the basal plane (2.950 Å). The ratio of the three bond integrals is fixed by canonical band theory [70], namely ddσ:ddπ:ddδ = −6:4:−1. The magnitude of the integrals is chosen to give the correct d-band width for titanium, 6.08 eV [71]; this implies ddσ(r_0) = −0.689 eV, ddπ(r_0) = 0.459 eV, ddδ(r_0) = −0.115 eV. Furthermore, in order to assure that the calculations remain within a reasonable computational time and memory requirements, a cut-off radius, $r_{\text{cut}} = 4.4$ Å, has been introduced that cuts off just before the third nearest neighbours. In order to guarantee that the bond integrals decrease smoothly to zero, the third order polynomial is employed for 3.1 Å $< r_{IJ} <$ 4.4 Å instead of the power law function (Eq. (37)). The coefficients in the cubic splines, which are computed automatically in the OXON code, are chosen so that the polynomial and its first derivative are equal to the values given by Eq. (37) for $r = 3.1$ Å (just beyond the first neighbour distance) and zero for $r = 4.4$ Å (just inside the third nearest neighbour distance).

The number of exact recursion coefficients included in the BOP expansion was chosen to ensure that the correct relative ordering of the energies of the hcp, fcc and bcc structures was obtained. This requires including terms up to the third level in the continued fractions (i.e. including b_2 and a_2 in Eq. (5) or the sixth and seventh moments exactly). We have,

therefore, taken our BOP expansion to one further level beyond this minimum required for the prediction of cubic versus hexagonal-close-packed stability or, equivalently, the value of the stacking fault energy. Consequently, our potential has all moments exact up to and including the ninth. We have chosen a band filling of $N_d = 2$ that gives the correct relative ordering of fcc and bcc with respect to the ground state hcp structure (see Fig. 8.20 of [23]). As explained above, the effective electronic temperature T_e was introduced such that $k_B T_e = 0.3$ eV. Analytic Hellmann–Feynman forces then agree with numerical differentiation of the total energy to better than 0.0006 eV Å^{-1}.

In the construction of BOP for titanium the 'core' contribution, E_{core}, was not included and thus Cauchy pressures are not reproduced precisely. However, the exponent n_a in Eq. (37) was chosen such that the error in determination of both Cauchy pressures is very similar. This corresponds to $n_a = 3.5$ which is close to the exponent expected for metals at the beginning of the transition series. The functional form of the pair potential has been taken as

$$V(r_{IJ}) = \sum_{k=1}^{6} A_k (r_k - r_{IJ})^3 H(r_k - r_{IJ}) + A \frac{(r_s - r_{IJ})^3}{r_{IJ}^{3.5}} H(r_s - r_{IJ}) \qquad (47)$$

with $r_s = 2.80$ Å. In this formula a strongly repulsive core is added to the sum of cubic splines (Eq. (46)) at atomic separations well below the nearest neighbour spacing (2.90 Å). This part was determined so as to follow closely the universal equation of state [72–74] for compressions up to 20%; this leads to $A = 100$ eV $\text{Å}^{1/2}$. This part of the pair potential does not contribute to any of the equilibrium properties. While keeping the bond part of the energy fixed, the parameters r_k and A_k of the pair potential, presented in Table 2, have been determined by fitting the quantities summarised in Table 3.

The first important test of the potential is that the fitted equilibrium structure is stable relative to alternative crystal structures with different symmetry, in particular those with a similar packing, such as fcc and bcc structures. This has been assured by the choice of the number of valence d-electrons, $N_d = 2$. In both cases the cohesive energies are higher than

Table 2
Parameters of the pair potential for titanium BOP

k	A_k (eV)	r_k (Å)
1	−0.32351453540823	5.16
2	0.30102314441033	5.04
3	0.37996053212667	4.51
4	−0.96726987948604	4.12
5	0.87821096325361	3.93
6	1.32392864734672	3.25

Since polynomial splices represent the pair potential the coefficients A_k must be given with the precision of 14 figures in order to achieve an entirely smooth transition between different splices. The same applies in Tables 7, 10 and 14.

Table 3
Experimental quantities of titanium fitted: binding energy per atom (eV), lattice parameters (Å), elastic moduli (eV Å^{-3})

E^B	a	c/a	C_{11}	C_{33}	C_{44}
4.85	2.950	1.587	1.099	1.189	0.317

for the hcp structure: in the fcc case by 0.030 eV/atom and in the bcc case by 0.074 eV/atom. The DFT-based calculations [75] employing the full potential LMTO method [76] lead to somewhat larger differences, namely 0.092 eV/atom and 0.128 eV/atom, for fcc and bcc structures, respectively.

Since only three elastic constants have been fitted exactly, the first test of the potential is how well the remaining moduli, C_{12}, C_{13} and C_{66} (equal to $(C_{12} - C_{11})/2$) are reproduced. The calculated values of these elastic constants (in eV Å^{-3}) are $C_{12} = 0.462$, $C_{13} = 0.520$ and $C_{66} = 0.319$ and the experimental values are 0.542, 0.426 and 0.281, respectively. Hence, these elastic constants are reproduced to ± 0.1 eV Å^{-3}. The discrepancy is, of course, related to the precision with which the bond part reproduces the Cauchy pressures and they could be reproduced exactly if the E^{core} were included.

Since the elastic moduli are positively definite the hcp structure is stable with respect to arbitrary small homogeneous deformations. However, in crystal defects large distortions of the local environment away from equilibrium are present and thus it is important that the ideal lattice structure is also stable with respect to large distortions. While this can never be fully examined, the most important tests are stability with respect to large shears parallel to some low index crystal planes and stability with respect to large homogeneous strains. The former is tested in calculations of γ-surfaces, energy versus shear displacement surfaces for certain crystallographic planes. Their calculation and significance are discussed in more detail in the section dealing with application of the potentials. Here we just note that γ-surfaces for basal and prism planes are all positive and thus the potential guarantees the mechanical stability of the hcp structure with respect to large shears in these planes. Stability with respect to large homogeneous strains has been tested by calculating the energy as a function of homogeneous expansions and contractions (by $\pm 20\%$) in the close-packed directions in the basal plane ($\langle 11\bar{2}0 \rangle$) and in the c direction ($\langle 0001 \rangle$), respectively. The only minimum found corresponds to the fitted equilibrium values of the lattice parameters and thus no instabilities or metastable configurations occur for the range of deformations studied (for more details see [48]).

4.2. BCC molybdenum [49]

As in the case of titanium, only d-electrons that determine the stability of the bcc crystal structure were included in E^{cov} and thus only the ddσ, ddπ and ddδ two-centre bond integrals are involved. Since the bcc lattice is not a closed packed structure and the second neighbours are close to the first neighbours, the screening of the bond integrals is an essential ingredient. The dependence of the screened bond integrals, $\tilde{\beta}_\tau$, on the separation of atoms was evaluated numerically for different volumes of the unit cell using the first-principles TB-LMTO method [77]. The calculated bond integrals display a marked discontinuity between first and second nearest neighbours [49] and this is captured by including their screening arising from the non-orthogonality of the orbitals. This requires the introduction of parameters that enter the screening function defined by Eqs. (39)–(42). Specifically, these are the bond integral $\beta_{\text{sd}\sigma}$ (since the screening is assumed to be due to the s-valence electrons on the atoms neighbouring to the bond) and the overlap integral $O_{\text{sd}\sigma}$ together with the dd overlap integrals O_τ, where τ corresponds to σ, π and δ, respectively. The overlap integrals have the same scaling dependencies as the corresponding unscreened bond integrals so that they are also represented by the generalised GSP function (Eq. (37)) with the same parameters r_c, n_a, n_b and n_c as for the non-screened bond integrals β_τ. These

Table 4
Parameters for the screened bond integrals for molybdenum

	r_c (Å)	$\beta_\tau(r_0)$ (eV)	$O_\tau(r_0)$	n_a	n_b	n_c
ddσ	1.873	−1.6200	0.0442	0.79	0.79	4.426
ddπ	0.590	0.8900	−0.0352	0	1	1
ddδ	0.500	−0.1360	0.0253	0	1	1
sdσ	0.850	−1.1547	0.1600	0	1	1

parameters are summarised in Table 4. Additional fitting parameters, A_τ, appear in both the interference and second moment contributions to the screening in Eqs. (39)–(42) and they were chosen as $A_\sigma = A_\pi = 1$ and $A_\delta = 0.32$. The nearest neighbour equilibrium spacing was taken as $r_0 = 2.7256$ Å.

Magnitudes of bond and overlap integrals decrease rapidly with increasing interatomic distance and in bcc structures only first and second nearest neighbour contributions are significant. Hence, both the bond and overlap integrals have been cut-off between the second and third neighbours. In order to guarantee that the bond and overlap integrals decrease smoothly to zero, the GSP function is employed for $r < r_1$ and is augmented with a polynomial of fifth order for $r_1 < r < r_{\text{cut}}$. The coefficients of the polynomial are computed automatically in the OXON code so that the function and its first and second derivatives are continuous at $r = r_1$ and zero at $r = r_{\text{cut}}$. r_1 and r_{cut} were taken to be the same for all the bond and overlap integrals, specifically 3.3 Å and 4.3 Å, respectively. The analytic screening function reproduces very closely the bond integrals determined by the TB-LMTO with a large discontinuity between the first and second nearest neighbours in ddπ and ddδ bond integrals but only a small discontinuity in ddσ [49].

Similarly as in the case of titanium, nine moments of the density of states (four levels of Lanczos recursion) are used in calculations of the bond order. This guarantees that all the important features of the density of states, in particular the bimodal behaviour and pseudogap, are correctly reproduced. The d-band filling of $N_d = 4.2$ was used which is not too far from the value suggested by DFT-based calculations. Molybdenum comprises six valence electrons that are distributed between the nearly-free electrons sp-band and the tight-binding d-band and due to hybridisation N_d is not integer. However, the effect of sp-valent electrons is not ignored. Since nearly-free electrons possess no angular character the sp-valence electrons are implicitly included both in E^{core} (reflecting their exclusion from the sizeable ion core regions in transition metals) and in pair potential.

The contribution, E^{core}, was described by Eqs. (43) and (44) with parameters fitted to reproduce $C_{12} - C_{44}$ which is the only Cauchy pressure in cubic structures. Since there are six adjustable parameters in E^{core} and only one fitted quantity, these parameters cannot be unique. Values of these parameters were chosen such that the embedding exponential function in Eq. (44) decreases to zero between the second and third neighbours in the bcc lattice and the parameter r_{core} corresponds approximately to the radius of the core electrons. Similarly as in the case of the bond integrals, a smooth polynomial cut-off tail was introduced in the embedding exponential function in Eq. (44). For $r_{\text{tail}} < r < r_{\text{cut}}$, this function is augmented by a polynomial of fifth order to ensure a smooth decay to zero. The values of all the parameters of E^{core} are listed in Table 5.

The pair potential, given by Eq. (46), with $k = 1$–4, is principally repulsive but in the present case it also has also an attractive region which reflects a weak attractive

Table 5
Parameters of E^{core} for molybdenum BOP

B (eV Å)	r_{core} (Å)	λ_0 (Å^{-1})	C (Å^{-m})	v (Å^{-1})	m	r_{tail} (Å)	r_{cut} (Å)
118.3	0.8	2.0	110.0	2.0	2.0	3.30	4.40

contribution from the s–d hybridisation [49]. The quantities used to fit the pair potential are the cohesive energy, the lattice parameter and remaining elastic moduli; one elastic modulus has been fixed by the Cauchy pressure via E^{core}. They are listed in Table 6. The values of the node points, r_k, and coefficients, A_k, are summarised in Table 7. Recently, a strongly repulsive core was added to the sum of cubic splines, similarly as in Eq. (47), at atomic separations well below the nearest neighbour spacing (2.725 Å). This part of the pair potential, which has not been included in Ref. [49], was determined so as to follow closely the compressive part of the universal equation of state [72–74]. Its functional form is

$$80 \frac{(r_s - r_{IJ})^{3/2}}{r_{IJ}^4} H(r_s - r_{IJ}) \quad \text{with } r_s = 2.6 \text{ Å} \tag{48}$$

The first requirement for the validity of the constructed potential is the stability of the ground state bcc structure relative to alternative crystal structures. This has been tested by calculating energies of the A15, fcc, hcp and simple cubic (sc) structures relaxed to their equilibrium densities using the BOP and comparing the results with calculations made by the DFT LMTO-ASA based method [66]. These results show that not only is the bcc structure most stable but that BOP reproduces well most structural energy differences found by DFT [49]. The addition of the term (48) improves the agreement for the sc structure.

γ-surfaces evaluated for {1 1 0} and {1 1 2} planes are all positive and thus the potential guarantees the mechanical stability of the bcc structure with respect to large shears in these planes. However, to test the applicability of the potential for the atomic environment considerably different from that in the ideal lattice highly distorted structures encountered along tetragonal, trigonal and hexagonal transformation paths [49,78] were investigated. The energy was calculated as a function of parameters characterising these paths using the constructed BOP and compared with the analogous calculations made by the *ab initio* FLAPW method [79,80]. In general, BOP reproduces the *ab initio* data closely and traces

Table 6
Properties of molybdenum fitted by the pair potential: lattice parameter (Å), binding energy per atom (eV) and elastic moduli (10^{11}Pa)

a	E^{B}	C_{11}	C_{12}	C_{44}
3.1472	6.82	4.647	1.615	1.089

Table 7
Parameters of the pair potential for molybdenum BOP

k	A_k (eV Å^{-3})	r_k (Å)
1	−0.078579421940	4.60
2	1.388283563938	3.70
3	5.235057880439	3.10
4	−5.990552025133	3.00

correctly even certain subtle features that originate from the directional character of the bonding. An example is the occurrence of two energy minima in the vicinity of the fcc structure along the trigonal path; for the fcc structure the energy then reaches a local maximum. It should be emphasised here that in contrast to BOP, central-force potentials give only one local minimum for the trigonal path, corresponding to the fcc structure [81].

Another test that probes the applicability of potentials in a locally disordered environment is the study of a vacancy. This crystal defect was modelled using periodic boundary conditions in all directions with the repeat cell of the size $3a \times 3a \times 3a$, where a is the lattice parameter, containing a total of 53 atoms. The atomic configuration was fully relaxed under the condition of constant volume. The vacancy formation energy calculated using the BOP is 3.5 eV. This compares well with *ab initio* results and experimental data that lie in the range 2.9–3.2 eV ([82–84] and references therein).

A thorough test of the potentials is provided by a comparison of calculated phonon dispersion curves with experimental data since the phonon spectra provide a wealth of information over all length scales – at long wavelengths the elastic properties of the lattice are examined while at short wavelengths the nature of interatomic bonding is directly probed. For this purpose phonon spectra were computed using the method of frozen phonons [85] for three high symmetry directions, specifically $[\zeta 0 0]$, $[\zeta \zeta \zeta]$ and $[\zeta \zeta 0]$. Despite some minor quantitative discrepancies, the agreement is satisfactory for all three branches. At this point it should be noted that the screening of the ddπ and ddδ bond integrals is essential for the $[\zeta \zeta 0]$ branch. Without screening the longitudinal and transverse mode (polarisation along $[0 0 1]$) phonons at the zone edge are much softer than experiments suggest. A detailed discussion of the effect of screening is found in [81].

4.3. FCC iridium [50,51]

The rationale for developing the BOP for iridium is the need for an appropriate description of atomic interactions in atomistic studies of dislocations and grain boundaries that may explain the exceptional mechanical behaviour of this fcc metal. Most notably, it is found that in tension single crystals of Ir fail by brittle transgranular cleavage after significant plastic deformation and in polycrystals both transgranular cleavage and intergranular fracture are failure mechanisms, again after significant plastic deformation [86–90]. Iridium is the only fcc metal to exhibit such mechanical behaviour that is most likely linked to the structure of dislocation cores. Furthermore, iridium has unusual elastic constants in that its Cauchy pressure, $C_{12} - C_{44}$, is small and negative [91]. In fact, iridium and the isoelectronic element rhodium [92] are the only cubic elemental metals to exhibit negative Cauchy pressures. Moreover, several anomalies are observed in the phonon spectrum of iridium [93].

As in other elemental transition metals, only d-electrons were included in E^{cov} and thus only the ddσ, ddπ and ddδ two-centre bond integrals are involved. However, calculations performed using a canonical d-band, where hybridisation between the d-electrons and the NFE sp-band is not included, do not predict that the fcc structure is favoured over the close-packed hcp structure, in particular for the number of d-electrons $N_d = 7.1$ that is given by fully hybridised spd LMTO calculation for iridium. This can be seen from Fig. 1 which shows that the fcc structure only becomes stable over hcp for $N_d > 7.5$. This problem was analysed in detail in Ref. [51] where it was found that sp–d hybridisation shifts this hcp–fcc node from 7.5 down to $N_d = 6.3$ without modifying the position of

the bcc–fcc nodes. Thus the d-electrons only model fails to account for the relative stability of fcc, hcp and bcc iridium. This deficiency could in principle be corrected by using the full spd basis in the development of the BOP but this would lead to an increase in the band width by a factor of around three and the use of this BOP in atomistic studies would be too demanding computationally as many more exact moments would be required for convergence. However, it was shown in Ref. [51] that the effects of hybridisation between the d-band and the NFE sp-band can be approximated to an excellent extent by a pairwise, central force term in the total energy. By terminating this pairwise term beyond third nearest neighbours in the fcc lattice, it could be parameterised such that it makes up the difference between the hcp–fcc energy difference calculated from E_{cov} and the value determined *ab initio*. In this manner, the total energies of the fcc and hcp structures are affected by the central-force term, but not the angular dependencies of interatomic bonding at short range.

The radial dependencies of the ddτ bond integrals were again determined using the first-principles TB-LMTO method and the integrals were represented analytically by the GSP function (Eq. (37)). Since the fcc structure is close-packed no screening of the bond integrals was included. The parameterisation of the corresponding GSP functions is summarised in Table 8. These bond integrals are cut-off at $r_{cut} = 4.3$ Å which is between second and third nearest neighbours in the fcc lattice and the polynomial cut-off tail, smoothly joined to the GSP function, is added at $r_1 = 3.3$ Å. The d-band filling of $N_d = 7.1$ electrons per atom was used that corresponds to iridium, as determined by LMTO calculations. Four levels of Lanczos recursion (nine moments) have again been employed in calculations of the bond order and the fictitious temperature used in calculations has again been taken such that $k_B T_e = 0.3$ eV.

The contribution, E^{core}, was described by Eqs. (43) and (44) with parameters fitted to reproduce the negative Cauchy pressure $C_{12} - C_{44} = -0.088$ eV Å^{-3}. The corresponding parameterisation is summarised in Table 9. The cut-off tail was again added to the embedding exponential function given by Eq. (44) for $r_{tail} < r < r_{cut}$.

The pair potential, given by Eq. (46) with $k = 1$–4, is used to fit remaining elastic moduli, the fcc lattice parameter and cohesive energy. Furthermore, the positions of the node points were selected so that the hcp–fcc structural energy difference calculated *ab initio* was reproduced. In this manner, as mentioned above, the pairwise central force interaction also represents the effects of the NFE–d hybridisation on the energy. The parameterisation of the pairwise term is presented in Table 10 and equilibrium properties of iridium fitted are summarised in Table 11.

Table 8
Parameterisation of the GSP functions for iridium ddτ bond integrals

	r_c (Å)	$\beta_\tau(r_0)$ (eV)	r_0 (Å)	$n_a = n_b$	n_c
ddσ	3.30	−1.35966	2.714583	1.75339	3.71958
ddπ	3.30	0.564208	2.714583	1.70200	5.32968
ddδ	3.30	−0.0646463	2.714583	1.83500	7.97587

Table 9
Parameters of E^{core} for iridium BOP

B (eV Å)	r_{core} (Å)	λ_0 (Å^{-1})	C (Å^{-m})	v (Å^{-1})	m	r_{tail} (Å)	r_{cut} (Å)
37.21	1.0	2.0	110.0	1.5	2.0	3.10	4.20

Table 10
Parameters of the pair potential for iridium BOP

k	A_k (eV Å^{-3})	r_k (Å)
1	1.621484180452	3.36945
2	−0.034464172823	4.40000
3	1.479986236465	5.23000
4	−1.300753052492	5.33000

Table 11
Physical properties of iridium fitted during parameterisation: lattice parameter (Å), binding energy per atom (eV), elastic moduli (eV Å^{-3}) and difference between the energy of the hcp and fcc structure per atom (meV atom^{-1})

a	E^{B}	C_{11}	C_{12}	C_{44}	E (hcp) − E (fcc)
3.839[a]	6.93[b]	3.620[c]	1.510[c]	1.598[c]	78.8

  [a] Ref. [89].
  [b] Ref. [94].
  [c] Ref. [91].

As in the previous cases, the first test of the BOP for iridium is evaluation of the relative stability of crystal structures other than fcc. The fcc–hcp energy difference was fitted during the construction of the potential but the transferability of the BOP to more open A15, bcc and simple cubic (sc) structures was tested. The calculation of the energy differences and equilibrium volumes using the BOP was compared with analogous *ab initio* calculations made using the mixed-basis, full potential augmented plane-wave plus local orbitals (APW+lo) method [79,95] as implemented in the WIEN2k package of codes [80]. The transferability of the BOP to the A15 and bcc structures is good: the energy differences and equilibrium volumes calculated using the BOP and *ab initio* are the same within 5%. The transferability of the BOP to the sc structure is less satisfactory with an error of around 12% in the equilibrium atomic volume. However, this is not of great concern since the energy of sc structure is so high that it is extremely unlikely that it would ever occur in extended defects. The key result of this test is that the BOP predicts the same increasing order of energies as *ab initio* calculations, i.e. fcc → hcp → A15 → bcc → sc.

γ-surface for the (1 1 1) plane is everywhere positive and thus the potential guarantees the mechanical stability of the fcc structure with respect to large shears in this close-packed plane. The symmetry dictated minimum on the γ-surface that corresponds to the intrinsic stacking fault determines the energy of this planar fault. The calculated value of the stacking fault energy, 408 mJ m^{-2}, is in an excellent agreement with experiment, 420 mJ m^{-2} [96], as well as with the range of values calculated *ab initio*, 365 [97] – 445 mJ m^{-2}. The vacancy formation energy, $E_{\mathrm{vac}}^{\mathrm{f}}$, was also calculated allowing for full atomic relaxation. $E_{\mathrm{vac}}^{\mathrm{f}}/ \mid E_{\mathrm{B}} \mid = 0.43$ is not in good agreement with the results of *ab initio* calculations that report $E_{\mathrm{vac}}^{\mathrm{f}}/|E_{\mathrm{B}}| = 0.27$ and 0.33 (Refs. [98] and [97], respectively). The origin of the discrepancy between the vacancy formation energy predicted by the BOP and those predicted by first-principles calculations is not clear. It is likely that the BOP is unable to account for local changes in electronic structure around the vacancy that are properly captured in DFT calculations [99].

In order to further test the applicability of the constructed BOP to atomic environments considerably different from that in the ideal lattice, calculations of the tetragonal and trigonal deformation paths were made, analogously as in the case of molybdenum. The

agreement between calculations employing the BOP and the *ab initio* method are outstanding. The transferability of the BOP to the bcc structure is very good but larger errors are seen for the sc structure, encountered along the trigonal path, as also mentioned previously. However, most notable is the agreement between the predictions of the BOP and *ab initio* calculations for the energy differences at intermediate points along both paths. For these points structures exhibit very little symmetry and this provides a high confidence for the transferability of the BOP to crystal defects where the local symmetry and related bond angles and coordination numbers may differ significantly from the fcc environment.

As a final test, the phonon spectra of iridium along the $[\zeta 0 0]$, $[\zeta \zeta 0]$ and $[\zeta \zeta \zeta]$ directions were calculated using the same frozen phonons method as for molybdenum [51]. The phonon spectra of iridium are particularly interesting since several anomalies are observed experimentally [93]. Specifically, in the $[\zeta \zeta 0]$ branches, local minima and inflexion points are found that cannot be accounted for by crystal symmetry arguments and are likely to be due to the strong angular character of interatomic bonding in iridium. The overall agreement between the calculations and experiment is excellent. Since the experimental elastic constants of iridium were fitted exactly, both sets of spectra are practically identical at long wavelengths. However, the agreement between experiment and theory at shorter wavelengths is also very good. A notable success of the BOP is its accurate prediction of the anomaly in the $[\zeta \zeta 0]$ T2 branch starting around $\zeta = 0.5$. As discussed in more detail in [51], the atomic displacements associated with this phonon mode couple to the angular character of interatomic bonding in iridium in a particularly strong manner, leading to the observed anomalies.

4.4. L1₀ TiAl [52]

The most promising high-temperature intermetallics are titanium aluminides based on γ-TiAl with the tetragonal L1₀ structure [100–103]. In structural applications, such as turbine engines, the most important properties are ductility and propensity to fracture at both ambient and high temperatures. The deformation modes in TiAl are relatively complex [104–106] and thus understanding of dislocation core structures and mechanisms of dislocation glide are an essential ingredient for understanding the ductility and/or brittleness of this alloy. This will be discussed more in the following section on the application of BOPs. Investigation of dislocations and related deformation modes is the primary rational for the development of BOPs for TiAl. While several central-force potentials were constructed and employed in such studies [78,107,108], none of them is able to reproduce the negative Cauchy pressures ($C_{13} - C_{44} = -0.213$ eV Å^{-3} and $C_{12} - C_{66} = -0.04$ eV Å^{-3} [109]) associated with the elastic moduli of these compounds, as well as a relatively high energy of the superlattice intrinsic stacking fault (SISF) on {1 1 1} planes. Both these features are linked with covalent bonding arising due to the partially filled d-band.

The bond energy given by Eq. (1) can be separated into three parts that correspond to Ti–Ti, Al–Al and Ti–Al interactions. The radial dependence of bond integrals that enter the TB Hamiltonian was again ascertained by applying the orbital downfolding method to data obtained from calculations employing screened TB-LMTO theory [110–112]. The angular dependencies are represented by the Slater–Koster form [57]. In constructing the BOPs a simple pd tight-binding model was employed in which only the d valence electrons on Ti and the p valence electrons on Al are retained explicitly in the attractive contribution E^{cov}. This approximation is sufficient to describe correctly the experimental structural trends within transition metal-metalloid binary compounds [23,113]. This leaves

seven types of bond integrals to be fitted: ddσ, ddπ and ddδ for the Ti–Ti interactions, ppσ and ppπ for the Al–Al interactions and pd(dp)σ and pd(dp)π for the Al–Ti (Ti–Al) interactions. The pd and dp bond integrals are equal to one another in the BOP formalism because the Hamiltonian matrix must be symmetric. Hence, the pd and dp bond integrals that enter the Hamiltonian are taken as averages of the fits to Ti–Al and Al–Ti bond integrals calculated *ab initio*.

Similarly as in the case of titanium, the radial dependence of the bond integrals is assumed to display a power law, which in the framework of Eq. (37) means $n_b = 0$ and n_a and r_0 are fitting parameters that are somewhat different for Ti–Ti, Al–Al and Ti–Al interactions. A fifth order polynomial is used to augment the power law in order to cut-off the bond integrals smoothly. This cut-off tail is added at R_1 equal to 3.1 Å for Ti–Ti and Al–Al interactions and to 3.0 for and Ti–Al interactions. It reaches zero at $R_{cut} = 4.8$ Å for all interactions. The parameterisation of the bond integrals is summarised in Table 12.

The many-body repulsive term, E^{core}, is given by Eqs. (43) and (44) and is parameterised to make up the difference between the Cauchy pressures predicted by the bond part and experimental values. Note that it is only necessary to define the fitting parameters for the Ti–Ti and Al–Al interactions as the Ti–Al and Al–Ti terms are constructed by either taking the geometric or arithmetic means of these parameters. A cut-off tail is added to E^{core} in the same manner as it was done for the radial dependence of the bond integrals. In this case, the Ti–Ti, Al–Al and Ti–Al terms were augmented by a polynomial of fifth order at a distance of $R_1 = 4.8$ Å that was terminated at $R_{cut} = 5.4$ Å. The parameterisation of E^{core} is summarised in Table 13.

The pairwise term in the BOP for TiAl, E^{pair}, is again used to fit the cohesive energy, lattice parameters and remaining elastic constants (the two Cauchy pressures in L1$_0$ TiAl are already fitted during the parameterisation of E^{cov} and E^{core}). This term has the form (45) with the pair potential, $V(r_{IJ})$, given by the polynomial form (46). However, this

Table 12
Parameters of bond integrals for the BOP for TiAl

	r_0 (Å)	$\beta_\tau(r_0)$ (eV)	n_a
ddσ(Ti–Ti)	2.9500	−1.1526	3.6
ddπ(Ti–Ti)	2.9500	0.5284	3.6
ddδ(Ti–Ti)	2.95	−0.0622	3.6
ppσ (Al–Al)	2.8320	1.8986	3.4
ppπ(Al–Al)	2.8320	−0.2255	3.4
dpσ (Ti–Al)	2.8547	−1.3970	2.7
dpπ(Ti–Al)	2.8547	0.3748	2.7

Table 13
Parameters of E^{core} for the BOP for TiAl

	Ti–Ti	Al–Al
B^{s_I} (eV)	183.0	10^5
$r_{core}^{s_I}$ (Å)	0.90	0.25
$\lambda_0^{s_I}$ (Å^{-1})	3.900	3.308
C^{s_I} (Å^{-1})	175.0	210.0
v^{s_I} (Å^{-1})	1.90	2.79
m^{s_I}	2.0	2.0

Table 14
Parameters in the pairwise terms of the BOP for TiAl: r_k ($k = 1$–6) in Å, A_k ($k = 1$–6) in eV Å^{-3} and r_N in Å

		Ti–Ti	Al–Al	Ti–Al
$k = 1$	r_1	3.30	2.90	3.00
	A_1	1.06358595447043	−47.49189347419121	2.71679815114202
$k = 2$	r_2	4.20	3.00	5.20
	A_2	17.56880739523064	21.70352401338154	0.27410330332275
$k = 3$	r_3	4.25	5.10	5.30
	A_3	−19.40798869407337	0.47293603817434	−0.20738373989069
$k = 4$	r_4	4.70	5.30	–
	A_4	−10.99281313250478	−0.30049982219861	–
$k = 5$	r_5	4.75	–	–
	A_5	30.61566487747791	–	–
$k = 6$	r_6	4.80	–	–
	A_6	−17.54485126799736	–	–
V_{aug}	r_N	2.75	2.75	2.75
V_{aug}	n_{aug}	3.3	3.5	3.5

Table 15
Properties of L1$_0$ TiAl calculated using the constructed BOP compared with experimental values: the binding energy (eV), the lattice parameters a and c (Å), taken from Ref. [114], and the elastic moduli (eV Å^{-3}), taken from Ref. [109]. The values of E^{B}, a, c, C_{33} and C_{44} were fitted exactly

	BOP	Experiment
E^{B}	−4.520	−4.520
a	4.005	4.005
c	4.06908	4.06908
c/a	1.016	1.016
C_{11}	1.135	1.167
C_{12}	0.427	0.467
C_{13}	0.474	0.467
C_{33}	1.136	1.136
C_{44}	0.680	0.680
C_{66}	0.473	0.507

polynomial form was augmented at separations somewhat smaller than the first nearest neighbours spacing by another pair potential

$$V_{\mathrm{aug}}(r_{IJ}) = \frac{\mathrm{d}V(r_{IJ})}{\mathrm{d}r_{IJ}}(r_{IJ} - r_N)\left(\frac{r_N}{r_{IJ}}\right)^{n_{\mathrm{aug}}} H(r_N - r_{IJ}) \tag{49}$$

At the same time the Ti–Ti pair potential was altered such that for 3.5 Å $< r_{IJ} <$ 4.5 Å $V(r_{IJ}) = -0.0411672808 \cdot (4.5 - r_{IJ})^3 + 0.1341241221 \cdot (4.5 - r_{IJ})^2$ and $V(r_{IJ}) = 0$ for $r_{IJ} >$ 4.5 Å. The reason for these modifications of pair potentials was to ensure that the L1$_0$ structure is more stable than the B19 structure.[1] The parameterisation of the pairwise terms in the BOP for TiAl is given in Table 14.

A comparison of experimental values of the cohesive energy, lattice parameters and elastic constants with those calculated using the constructed BOPs is presented in Table 15.

---

[1] The description of the modification of pair potentials was accidentally omitted in the paper [52] but it is essential for attaining the stability of the L1$_0$ structure.

None of the calculated values differs from experiment by more than 10%, which is a very adequate agreement for our purposes. However, note that some of the quantities were fitted exactly. Furthermore, in Ref. [52] the BOPs were also constructed for the case of $c/a = 1$. These differ only marginally from those for the exact value of c/a and are used in dislocation studies in order to attain the periodicity along the <101] directions.

The first test of the constructed BOPs was the calculation of the bonding energy as a function of homogeneous expansions and contractions of the two lattice parameters a and c by $\pm 20\%$. The resulting energy surface possesses only one minimum, at the fitted equilibrium values of a and c. Hence, within the tested deformation range, the potential does not lead to any instabilities or unphysical metastable configurations for non-uniform expansions or contractions of the lattice.

The second test is the study of the relative energy differences of alternative structures with the same composition as TiAl. The BOP predicts the increasing order of energies from $L1_0 \rightarrow B19 \rightarrow B2 \rightarrow B1$ in agreement with *ab initio* calculations [25,27]. In addition, studies of tetragonal, trigonal and hexagonal transformation paths [78] between the above structures, which can be found in [115], are in a satisfactory agreement with calculations performed using the *ab initio* FLAPW method. At the same time, calculations of γ-surface for {1 1 1} planes demonstrates that the potentials guarantee the mechanical stability of the $L1_0$ structure with respect to large shears in this close-packed plane.

A final test is the assessment of the transferability of constructed BOPs for TiAl to the 3:1 stoichiometry of Ti_3Al, which crystallises in the $D0_{19}$ structure The comparison between prediction and experimental [116] and density functional theory based calculated lattice parameters, cohesive energy and elastic constants [117] is very satisfactory considering that the BOPs were developed by fitting to the alloy with the 1:1 stoichiometry [52]. Furthermore, the energy difference between the two competing close-packed structures, hexagonal DO_{19} and cubic $L1_2$ is 4.2 meV/atom in favour of $D0_{19}$. Qualitatively, this compares well with the *ab initio* calculated energy difference of about 10 meV/atom.

5. Application of constructed bond-order potentials to studies of dislocation cores

While a broad variety of dislocation phenomena encountered in plastically deforming materials can be fully analysed in the framework of continuum elasticity (see, for example [118]), ample evidence now exists for a broad range of crystalline materials where the dislocation core structures significantly influence macroscopic plastic flow and may even be a governing factor (for recent reviews see [119–125]). The properties of the core region and its impact on dislocation motion and thus on plastic yielding, can only be fully understood when the atomic structure and its variation with applied stresses are adequately accounted for. Experimental studies of dislocation cores, such as high-resolution electron microscopy, are very limited (see, for example, [2,126–131]) and the major source of understanding of core phenomena is computer modelling. The essential precursor of such studies is an appropriate description of atomic interactions and this has been the main purpose of the development of BOPs described in this paper.

A vital characteristic of dislocations in crystalline materials is their possible dissociation into partial dislocations connected by stacking-fault-like defects that include not only stacking faults but also antiphase domain boundaries and complex stacking faults encountered in ordered alloys and compounds. These planar defects can be most conveniently analysed using the notion of γ-surfaces defined as follows [121,132]. Suppose that a crystal is

cut along a chosen crystal plane and the upper part displaced with respect to the lower part by a vector **u**, parallel to the plane of the cut. The fault created in this way is called the *generalised single-layer stacking-fault* and it is not in general metastable. The energy of such fault, $\gamma(\mathbf{u})$, can be evaluated when an appropriate description of atomic interactions is available. In such calculations relaxations perpendicular to the fault have to be allowed but no relaxations parallel to the fault are permitted. Repeating this procedure for various vectors **u** within the repeat cell of the selected crystal plane, an energy-displacement surface can be constructed, and this surface is commonly called the γ-surface. Local minima on this surface determine the displacement vectors of all possible metastable single-layer stacking-fault-like defects, and the values of γ at these minima are the energies of these faults. Moreover, the full shape of a γ-surface can be employed in semi-atomistic models of the Peierls–Nabarro type that are capable to describe planar dislocation cores with high precision [125,133–135]. However, in the case of non-planar cores, in particular when directional bonding dominates, only full atomistic modelling of dislocations is adequately reliable. The methods of computer simulation of straight dislocations have been outlined in a number of publications (see, for example [121,136]) and in this paper we summarise results of dislocation studies obtained using the BOPs described in the previous section.

5.1. Titanium [137]

In the hcp structure the most common dislocations mediating the plastic deformation are dislocations with the Burgers vector $\frac{1}{3}[\bar{1}2\bar{1}0]$. They can glide in both basal $(0\,0\,0\,1)$ and prism $(1\,0\,\bar{1}\,0)$ planes. The former is the principal slip plane in Be, Mg, Zn, Cd and Co, while the latter is strongly preferred in Ti, Zr, Hf, Y and a number of rare earth hcp metals [118]. As first noted by Legrand [138,139], the prism plane is generally favoured in transition metals and this preference may depend on the filling of the d-band. Indeed, it is the dominant slip plane in Ti, Zr and Hf which all have between 1.5 and 2.5 d-electrons, while in Co with more than eight d-electrons the basal slip dominates; in Re and Ru with six to seven d-electrons there is no clear preference for the basal or prism slip [140].

The splitting into partial dislocations and/or spreading of the dislocation core in a single crystallographic plane is generally the reason why such a plane is the dominant slip plane. In those hcp metals in which the basal slip dominates the $\frac{1}{3}[\bar{1}2\bar{1}0]$ dislocations, indeed, split into Shockley partials on the basal plane. Analogously, when the prism slip dominates we can expect that either splitting or spreading of the dislocation core into the prism plane is favoured. On the basal plane the metastability of the intrinsic stacking fault is guaranteed by symmetry [141] and, indeed, the calculated γ-surface possesses a minimum corresponding to the intrinsic stacking fault displacement $\frac{1}{3}[\bar{1}1\,0\,0]$. The energy of this fault is 110 mJ m^{-2}. This high stacking fault energy is a consequence of the distortion of the directional bonds between the first nearest neighbours. For central-force potentials the energy is controlled by interactions of third and more distant neighbours and thus the stacking fault energy is usually low. For example, the Finnis–Sinclair potential constructed for titanium by Ackland [142] gives the energy 64 mJ m^{-2}. No stacking fault is suggested by symmetry for the prism plane and the γ-surface for this plane, calculated using the BOP for Ti, does not display any minimum. Hence, no splitting into partials can be expected on the prism plane.

In order to study the core structure of $\frac{1}{3}[\bar{1}2\bar{1}0]$ dislocations the screw dislocation was investigated since it can spread into either basal or prism plane and even into both of them simultaneously. This dislocation was always found to spread into the prism plane,

independently of the starting configuration but a metastable configuration corresponding to the splitting on the basal plane could also be found if the partials were introduced via the starting configuration. These two core structures of the $\frac{1}{3}[\bar{1}2\bar{1}0]$ screw dislocation are shown using the differential displacement map in Fig. 3. In order to analyse the energetic preference for core spreading, we have compared their energies. The energy of a dislocation can be written as $E = (Kb^2/4\pi)\ln(R/R_{core}) + U_{core}$ where K is the appropriate combination of elastic constants, b the magnitude of the total Burgers vector, R the radial distance from the elastic centre, and R_{core} and U_{core} are the radius and energy of the core respectively, both of which cannot be defined uniquely [118]. Hence, the plot of the energy stored within the cylinder of radius R, centred on the dislocation line, versus $\ln(R/R_{core})$, will be a straight line for $R \gg R_{core}$ and the slope of this line is independent of the core structure. Such plots, evaluated using the corresponding relaxed blocks with the $\frac{1}{3}[\bar{1}2\bar{1}0]$ screw dislocation in the middle, demonstrate unambiguously that the dislocation with the core spread into the prism plane possesses a lower energy than the dislocation
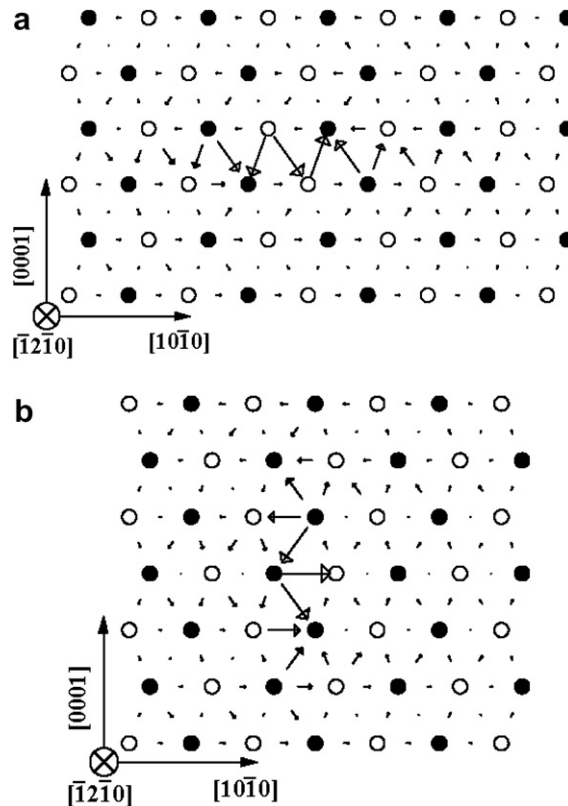

Fig. 3. Core of the $\frac{1}{3}[\bar{1}2\bar{1}0]$ screw dislocation in Ti calculated using the BOP. (a) Spread into the basal plane; (b) Spread into the prism plane. The circles depict atoms in the projection onto the plane perpendicular to the dislocation line and filled and empty circles distinguish two planes of atoms within one period $\left(\frac{1}{3}[\bar{1}2\bar{1}0]\right)$. The relative displacement parallel to the total Burgers vector (screw component) of the neighbouring atoms produced by the dislocation is depicted as an arrow between them. The length of the arrows is proportional to the magnitude of this displacement and it is normalised such that the length of the largest arrow is equal to the separation of the neighbouring atoms in the projection.

with the core spread into the basal plane [137,141]. This implies that in Ti (and presumably also Zr and Hf), the covalent directional bonding induced by the d-electrons, has a salient control over the core structure of dislocations in that spreading into the prism plane is preferred over splitting into the basal plane. It is then natural to conclude that the prism slip is favoured over the basal slip. However, this conclusion can only be definitive if it is shown that the dislocation glide in the prism plane is easier or at least equally difficult as in the basal plane. This requires evaluation of the Peierls stresses for both prism and basal planes, similarly as it was done in studies discussed below. One of the reasons such calculations have not been performed to date is that the BOP for titanium requires a further advancement by including the many-body repulsion, E^{core}, which was not included into the original development [48].

5.2. Molybdenum [49,143–146]

Distinguishing features of the plastic behaviour of bcc metals are controlled by the structure and properties of the cores of $1/2\langle 111 \rangle$ screw dislocations (for reviews see [119,147–150]). The most general reasons are crystallographic: First, $\langle 111 \rangle$ is the direction of a threefold screw axis in the bcc lattice and, second, unlike in fcc and hcp crystals, there are no symmetry dictated metastable stacking faults. Moreover, many γ-surface calculations concluded that no metastable stacking faults exist in bcc metals [49,83,119,132,151]. Hence, dislocations cannot dissociate in a planar manner as in fcc metals and thus the $\langle 111 \rangle$ screw dislocation will possess the threefold screw symmetry and is, therefore, intrinsically non-planar [152,153]. This suggests that screw dislocations are more difficult to move than dislocations of other orientations. However, crystallography alone does not say in what manner the core is spread in space and, even more importantly, how such a core responds to external loading. Consequently, investigation of this phenomenon is an outstanding topic for atomistic simulation in transition metals, such as Mo, in which the directional bonding mediated by d-electrons dominates cohesion. The BOP is an excellent description of atomic interactions for such studies.

A large number of simulations of dislocations in bcc metals have been made using a broad variety of descriptions of atomic interactions (for reviews see [119,154]). In all these studies the core was found to spread into three {1 1 0} planes, specifically $(\bar{1}01)$, $(0\bar{1}1)$ and $(\bar{1}10)$ for the $1/2[111]$ dislocation. The core structure found in the calculations employing the BOP for molybdenum is shown in Fig. 4a using the differential displacement map. The same structure was found in recent calculations employing a DFT-based *ab initio* method [155]. This core has a threefold symmetry, as required by the [1 1 1] threefold screw axis, and is also invariant with respect to another symmetry operation of the bcc lattice, the $[10\bar{1}]$ diad. In many previous calculations a configuration that is not invariant with respect to the latter symmetry operation was found. In this case two configurations related by the $[10\bar{1}]$ diad exist. In the [1 1 1] projection, which is usually used when depicting the core, the diad invariant structure appears as sixfold and the non-invariant structure as threefold. The particular core structure found in simulations obviously depends on the description of atomic interactions used. In molybdenum, and probably all other transition metals, as recently argued by Frederiksen and Jacobsen [151], the core structure of $1/2[111]$ screw dislocations is invariant with respect to the $[10\bar{1}]$ diad. In contrast, it is likely that in alkali metals the diad non-invariant structure dominates, as found in earlier studies employing the weak pseudopotentials to describe atomic interactions [119,156–159]. In both cases
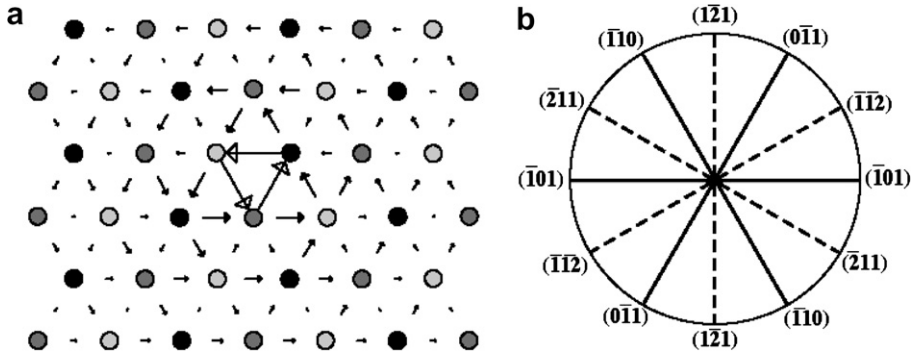
Fig. 4. (a) Core structure of the 1/2[1 1 1] screw dislocation in Mo calculated using the BOP. The atomic arrangement is shown in the projection perpendicular to the direction of the dislocation line ([1 1 1]) and circles represent atoms within one period; their positions in three successive (1 1 1) planes are distinguished by shading. The arrows have the same meaning as in Fig. 3. (b) [1 1 1] stereographic projection showing orientations of all {1 1 0} and {1 1 2} planes belonging to the [1 1 1] zone.

the core is non-planar and the screw dislocation is thus sessile. The corresponding Peierls stress is very high when compared, for example, with fcc metals and the glide of screw dislocations is, therefore, very difficult at low temperatures but can be aided by thermal activation at finite temperatures, which leads to a strong temperature dependence of the yield stress [119,150]. Moreover, the three-dimensional spreading of the cores of screw dislocations is also responsible for slip geometry that, in general, does not obey the Schmid law and leads to dependencies of the yield and flow stress on other components of the applied stress than the shear stress in the direction of the Burgers vector in the slip plane, i.e. the Schmid stress [143–146,154,158–160].

However, the above mentioned features of the dislocation motion are not determined solely by the symmetry of the cores of screw dislocations. In fact it has been shown that both the diad invariant and non-invariant cores may respond qualitatively in the same way to applied stresses while there may be significant quantitative differences between the cores of the same type but different descriptions of atomic interactions, i.e. different materials [145]. Hence, to understand, for example, the complex slip geometry in a given material the dislocation glide has to be modelled for this specific material. Again, this is enabled by BOPs that provide a physically reliable description of atomic interactions and allow at the same time the performance of the very large calculations needed for such studies.

Extensive investigations of the effect of applied stresses upon the core structure and related dislocation glide have been made using the BOP for Mo [49,143–146] and similar studies are in progress for W, Ta and Nb. The application of the pure shear stress parallel to the Burgers vector for different orientations of the maximum resolved shear stress plane (MRSSP) reveal a significant deviation from the Schmid law in that the critical resolved shear stress (CRSS) at which the dislocation moves depends on the sense of shearing. This asymmetry, however, still relates to the crystal symmetry since the (1 1 1) plane is not the plane of a mirror symmetry in the bcc lattice and thus there is no reason why shearing in the positive and negative [1 1 1] direction should be the same. This asymmetry, previously identified with the twinning–antitwinning asymmetry of shearing along {1 1 2} planes, is thus general for all bcc metals. However, no symmetry argument decides how significant this asymmetry is and whether shearing should be more difficult in the twinning or

antitwinning sense but calculations employing various descriptions of atomic interactions all find that it is easier in the twinning sense. This finding is in full agreement with experiments [119,147,150,161,162]. However, the interesting results of calculations employing the BOP for Mo is that this asymmetry of yielding is not the only one and, in fact, asymmetries induced by stresses that are perpendicular to the Burgers vector may be even more significant. This is clearly reflected in calculations investigating the effect of applied tensions and compressions [144–146]. A strong tension–compression asymmetry of the CRSS is found for the same orientation of the MRSSP. If the dislocation motion were controlled solely by the shear stress parallel to the Burgers vector such asymmetry would not exist. This effect is most pronounced when the MRSSP is the $(\bar{1}01)$ plane since no asymmetry based on the twinning–antitwinning asymmetry exists for this orientation. Such tension–compression asymmetry was, indeed, observed in molybdenum for this orientation of the MRSSP [162].

In order to decipher which stress components affect CRSS, the influence of shear stresses perpendicular to the Burgers vector was studied, as proposed in [163], in a manner useful for understanding tension and compression. For a given MRSSP this is achieved by applying the stress tensor with the components $\sigma_{11} = -\tau$, $\sigma_{22} = \tau$, $\sigma_{33} = \sigma_{12} = \sigma_{13} = \sigma_{23} = 0$ in the right-handed coordinate system with the x_1 axis in the MRSSP, x_2 axis perpendicular to the MRSSP and x_3 axis parallel to [111]. In this way we attain shear stresses in the {110} planes of the [111] zone perpendicular to the Burgers vector and a direct link with the studies of tension and compression can be made [146,163]. Fig. 5 shows the calculated dependence of the CRSS on τ when the $(10\bar{1})$ plane is the MRSSP. It is important to note that changing the sign of τ corresponds to the rotation of the coordinates by 180° around the [111] axis. However, the core structure is not invariant with respect to this transformation and thus the effect of τ upon the dislocation behaviour is, in general, different for positive and negative values of τ. When compared with tensile/compressive tests, positive τ corresponds to tension and negative to compression. The values of the CRSS for tension/compression along the $[\bar{2}38]$ and $[012]$ axes, for which the MRSSP is the $(\bar{1}01)$ plane, are also shown in Fig. 5. The CRSS is lower for tension than compression. This tension–compression asymmetry that cannot be induced by the twinning–antitwinning asymmetry is in excellent agreement with observations in Ref. [162]. The almost perfect fit of the
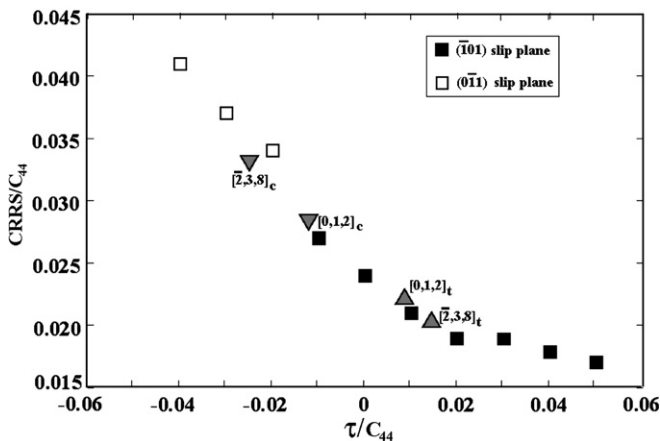

Fig. 5. Dependence of the CRSS on τ, calculated using the BOP for Mo, when the $(10\bar{1})$ plane is the MRSSP.

results of tensile/compressive tests onto the CRSSS versus τ dependence demonstrate that it is the shear stress perpendicular to the Burgers vector that controls the significant differences between tension and compression. These findings are important when formulating yield criteria for the use in continuum crystal plasticity and, eventually, in continuum studies of deformation of polycrystals. Until recently such criteria were usually based on the Schmid law whilst the atomic level studies described here suggest, on a firm physical basis, which other stress tensor components have to be included in order to describe the plastic behaviour of a specific material accurately on the continuum level [143,144,146].

It is seen from Fig. 5 that the shear stress perpendicular to the Burgers vector affects considerably not only the magnitude of the CRSS but it can even lead to the change of the slip plane. For large enough negative τ the slip plane is $(0\bar{1}1)$ although the MRSSP is $(10\bar{1})$. This finding may explain the anomalous slip behaviour observed in Mo deformed in compression at low temperatures [164]. The most prominent slip system observed in [164] is $(0\bar{1}1)/[111]$ although the Schmid factor is only 65% of that for the slip system $(10\bar{1})/[111]$. In addition, there are two more possible slip systems, $(101)[\bar{1}11]$ and $(011)[\bar{1}\bar{1}1]$, with Schmid factors 27% larger than the $(0\bar{1}1)/[111]$ system. The reason for such significant influence of the shear stress perpendicular to the Burgers vector on both the magnitude of the CRSS and slip geometry is the change in the core structure induced by this stress. While this effect is likely to occur in all bcc metals, it can vary significantly from metal to metal and thus a reliable description of atomic interactions, such as BOPs, is essential for its investigation.

5.3. Iridium [50]

Using the constructed BOP for iridium atomistic simulation of the $\frac{1}{2}[1\bar{1}0]$ screw dislocation was carried out. Similarly as in the case of titanium, the screw dislocation was investigated since it can spread into two different planes, (111) and $(11\bar{1})$ of the $[1\bar{1}0]$ zone and even into both of them simultaneously. Two different core structures, shown in Fig. 6, have been found. The first core (Fig. 6a) is planar and corresponds to the dissociation into two Shockley partials separated by the intrinsic stacking fault. This structure is the same as found in all fcc metals though owing to the high stacking fault energy (408 mJ m^{-2}) the splitting is very narrow, which we estimate to be about 12 Å. The second core (Fig. 6b) is non-planar, spread into the intersecting (111) and $(11\bar{1})$ planes. The analysis of the energies of dislocations possessing these two distinct core structures showed that the non-planar core is metastable since the energy of the dislocation with this core is about 0.33 eV/b higher than that of the dislocation dissociated into Shockley partials. The energies of the two configurations become equal when the dissociated dislocation is constricted to a splitting of around 7 Å. Such a constriction can be attained within a pile-up or with the help of shear stresses perpendicular to the Burgers vector, as first pointed out by Escaig [165].

As in the case of Mo, understanding the role these two core structures may play in the deformation behaviour requires simulation of the effect of applied stresses and thus the glide of dislocations. In the case of the planar core it was found that the CRSS at which the dislocation starts to glide along the (111) plane, i.e. the Peierls stress, is $2 \times 10^{-4} C_{44}$. This low value confirms that the dislocation with the planar core is a highly glissile. The simulations of the effect of stresses parallel to the Burgers vector upon the dislocation with the non-planar core showed that the core transforms into the glissile planar configuration at an applied stress of $8 \times 10^{-5} C_{44}$. However, an important finding is that if a very small stress
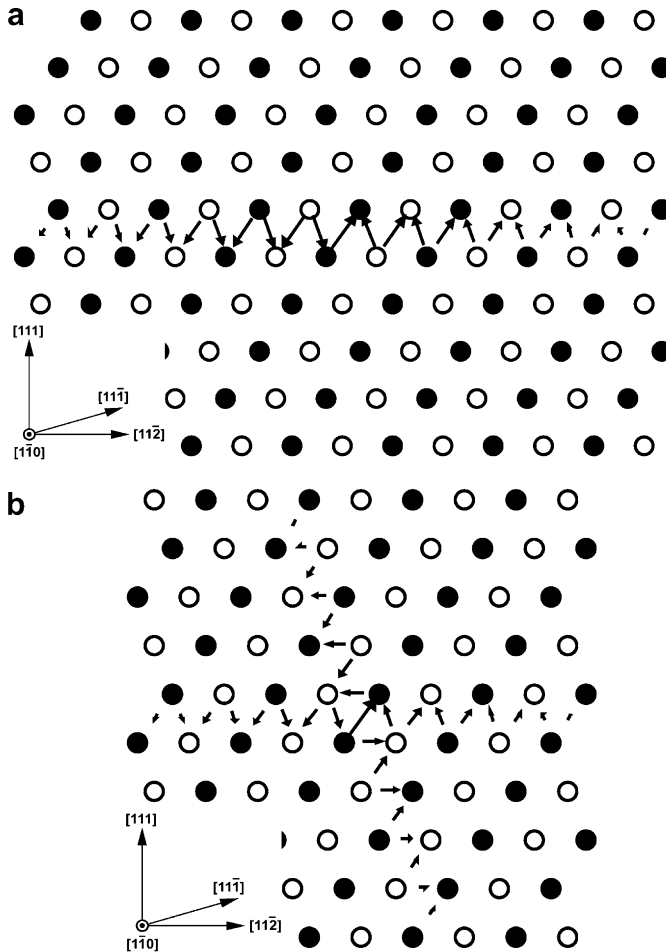
Fig. 6. The core structures of the $\frac{1}{2}[1\bar{1}0]$ screw dislocation in iridium. (a) Planar spread into the (1 1 1) plane. (b) Non-planar spread into (1 1 1) and (1 1 $\bar{1}$) planes. The circles depict atoms in the projection onto the (1 $\bar{1}$ 0) plane perpendicular to the dislocation line. Filled and empty circles distinguish two planes of atoms within one period. The arrows have the same meaning as in Fig. 3. Configuration (b) also represents the core of the ordinary $\frac{1}{2}[1\bar{1}0]$ screw dislocation in TiAl but the open and filled circles now represent Al and Ti atoms, respectively.

perpendicular to the Burgers vector, somewhat larger than $5 \times 10^{-5} C_{44}$, was superimposed on the shear stress driving the glide, this transformation took place into the cross-slip plane (1 1 $\bar{1}$) rather than the primary plane (1 1 1). Hence, unlike in bcc metals, the screw dislocation with non-planar core is not an obstacle inhibiting the motion of dislocations.

However, the non-planar core may play an important role in the cross-slip which can then occur without the aid of thermal activation. The reasons for such a process are the following: The transformation from the planar to the non-planar core can be driven entirely by stresses that reduce the separation between Shockley partials. Such stresses can be provided by a dislocation pile up with a small number of dislocations. This transformation takes place without fully constricting the partials in the primary plane as the two configurations become energetically equivalent when the two partials are still well separated.

Once the non-planar core configuration is formed, it will immediately transform back into a planar core but on the cross-slip plane since there are always present stresses perpendicular to the Burgers vector favouring the cross-slip plane. Hence, the non-planar core should be considered as an intermediate configuration with a very short lifetime that facilitates cross-slip which can occur purely under the effect of applied stresses. Such athermal cross-slip may occur over long segments of screw dislocations with great frequency even at low temperature and the consequence is generation of Frank–Read sources via the double cross-slip mechanism [118]. These sources can rapidly generate large numbers of dislocations and we propose that a feedback mechanism exists in plastically deforming iridium whereby athermal cross-slip leads to the generation of Frank–Read sources that serve to generate glissile dislocations which in turn may cross-slip at any temperature to form new Frank–Read sources [50,166]. Hence, athermal cross-slip offers a pathway for the anomalously high rates of dislocation multiplication and thus a very high and spatially homogeneous density of dislocations and homogeneous neck free deformation, as observed in plastically deformed iridium [167]. The transgranular or intergranular fracture occurring after extensive plastic deformation is then a consequence of severe work-hardening associated with the large homogeneous plastic deformation.

It is notable that the model explaining the unique mechanical behaviour of iridium was inspired by the results of atomistic simulations employing the quantum mechanically derived, accurate and transferable BOP that describes interatomic bonding in this metal. This study demonstrates that the complex interplay between interatomic bonding with strong angular character and the structures of dislocations can lead to unusual mechanical behaviour.

5.4. γ-TiAl–L1$_0$ structure [52,168]

The main deformation modes in γ-TiAl are slip and twinning, both of them operating on the close-packed {1 1 1} planes (see, for example, [104,169]). The slip is mediated by two types of dislocations: ordinary dislocations with Burgers vectors 1/2 ⟨1 1 0] and superdislocations with Burgers vectors ⟨1 0 1]. While the underlying crystallography of the L1$_0$ structure is very close to fcc the deformation behaviour is much more complex. For example, different deformation modes occur in the single phase γ-TiAl depending on temperature [104,105]. Specifically, ⟨1 0 1] superdislocations dominate at low temperatures while at high temperatures (above about 800 °C) slip by 1/2 ⟨1 1 0] ordinary dislocations, and also twinning, become controlling deformation modes. Understanding of these deformation properties cannot be achieved in the framework of the standard dislocation theory since the core phenomena are again likely to play an important role and these require comprehension at the atomic level. Since the bonding in TiAl is mixed metallic and covalent, as documented by DFT-based calculations [25,27,170–172], the description of atomic interactions used in such calculations has to include adequately the directional bonding resulting from d–d and d–p bonds. This is achieved in the BOP described above.

The γ-surface for the (1 1 1) plane, calculated using the BOP [52], possesses three minima corresponding to the antiphase boundary (APB) with the displacement vector $\frac{1}{2}[1\,0\,\bar{1}]$, complex stacking fault (CSF) with the displacement vector $\frac{1}{6}[1\,\bar{2}\,1]$ and superlattice intrinsic stacking fault (SISF) with the displacement vector $\frac{1}{6}[1\,1\,\bar{2}]$. The energies of these faults are 545 mJ m^{-2}, 412 mJ m^{-2} and 140 mJ m^{-2}, respectively. These values agree well with those calculated using DFT-based methods [173,174]. In particular, the relatively high

energy of the SISF is reproduced correctly. It results from the change in the bond energy due to the angular dependence of first nearest neighbour bonds, while in central force models, which always lead to a too low value, only the third and more distant neighbours contribute to this energy. It should be noted that while the metastability of the SISF is guaranteed by the symmetry of the $L1_0$ structure, this is not the case for the APB and CSF (see e.g. [175]).

Dislocations studied atomistically using the BOP for TiAl were again screw dislocations because their slip plane is not defined uniquely [168]. The core of the ordinary $\frac{1}{2}[1\bar{1}0]$ screw dislocation was found to be spread symmetrically into two {111} planes, specifically (111) and $(11\bar{1})$. In terms of the differential displacements this core is again depicted by Fig. 6b but filled and empty circles now represent the positions of Al and Ti atoms, respectively. The same core structure was also found in *ab initio* calculations of Woodward and Rao [176]. In principle, a planar configuration corresponding to the dissociation into Shockley partials separated by the complex stacking fault (CSF) could exist but the non-planar core is the only structure found. The reason is, apparently, the very high energy of the CSF for which the splitting would be smaller than one lattice spacing. The glide of this dislocation was investigated by applying shear stress parallel to the Burgers vector. The core first partially constricts and the dislocation starts to move along either the (111) or $(11\bar{1})$ plane, depending on orientation of the MRSSP. The CRSS (Peierls stress) for the glide on the (111) plane is in excess of $0.02C_{44}$. This core behaviour and the magnitude of the Peierls stress are very similar to those of screw dislocations in Mo and other bcc metals. Thus the yield stress can also be expected to be strongly temperature dependent and the Schmid law will not be obeyed when the plastic deformation is mediated by ordinary dislocations. This is, indeed, what is observed and at low temperatures ordinary dislocations do not participate in the deformation process.

Atomistic modelling of the $[10\bar{1}]$ superdislocation in the screw orientation revealed two possible core structures, one planar and the other non-planar, both of which can be interpreted as splitting into partial dislocations. The planar configuration corresponds to the dissociation according to the reaction $[10\bar{1}] = \frac{1}{6}[11\bar{2}] + \frac{1}{2}[10\bar{1}] + \frac{1}{6}[2\bar{1}\bar{1}]$ with the superlattice intrinsic stacking fault (SISF) between the partials $\frac{1}{6}[11\bar{2}]$ and $\frac{1}{2}[10\bar{1}]$ and the CSF between the partials $\frac{1}{2}[10\bar{1}]$ and $\frac{1}{6}[2\bar{1}\bar{1}]$. The non-planar configuration corresponds to the dissociation according to the reaction $[10\bar{1}] = \frac{1}{6}[11\bar{2}] + \frac{1}{3}[20\bar{1}] + \frac{1}{6}[1\bar{1}\bar{2}]$ with the SISF on both (111) and $(1\bar{1}1)$ planes. This configuration, akin to the Lommer–Cottrell lock found in fcc materials [118], is completely immobile and can only act as an obstacle to the dislocations motion.

When applying the shear stress in the (111) plane in the $[10\bar{1}]$ direction to the superdislocation with the planar core it always transformed into the non-planar form if the $\frac{1}{6}[11\bar{2}]$ partial bounding the SISF would be leading during the glide. The superdislocation thus became completely locked. In contrast, when the shear stress was applied such that the $\frac{1}{6}[11\bar{2}]$ partial would be trailing, the core remained planar and the superdislocation started to move at the stress of $0.006C_{44}$, which is a relatively low Peierls stress. This difference in the sense of shearing leads to an interesting asymmetry. It can be expected that the yield stress will be higher when the partial bounding the SISF, $\frac{1}{6}[11\bar{2}]$, is leading than when it is trailing. This has, indeed, been observed in TiAl single crystals oriented for single slip [105,177,178].

In summary, modelling of dislocations in TiAl using the BOP explains the basic characteristics of slip in the single crystals of this compound. At low temperatures the superdislocations dominate since their cores can be planar and their Peierls stress signifi-

cantly smaller than that of ordinary dislocations. At the same time the calculations reveal a possible asymmetry in the glide of superdislocations. At high temperatures the ordinary dislocations, the cores of which are non-planar, can glide easily with the aid of thermal activation while such activations may enhance transformations of the cores of superdislocations into the sessile form. As mentioned above, experimental studies indeed confirm that superdislocations dominate at low temperatures and ordinary dislocations at high temperatures. It should be noted, similarly as in the case of iridium, that it is the directional character of bonding that is responsible for the important core features. For example, the core of the ordinary dislocation is non-planar owing to the very high energy of the CSF that results due to directional bonding of first nearest neighbours. However, the calculations summarised here are only the first step towards understanding the mechanical behaviour of TiAl based compounds. The most interesting are the titanium rich alloys exhibiting a two-phase lamellar structure, consisting of majority layers of $L1_0$ TiAl and minority layers of hexagonal, DO_{19} Ti_3Al [100,102,104]. Interaction of dislocations with interfaces between differently oriented TiAl lamellae, as well as interfaces between TiAl and Ti_3Al, are of principal interest [179–182] and atomistic study of these phenomena, which is presently in progress [183], represents a notable challenge for the BOPs.

6. Conclusions

The methodology of BOPs links systematically between the electronic and atomistic modelling hierarchies. This real-space description of interactions between the atoms, which is based on the tight-binding approximation to the electronic structure, is capable of treating mixed metallic and covalent bonding common in transition metals and their alloys. This is crucial for atomic level modelling of extended defects in these materials since the angular character of the bonding may govern both their structures and properties. The distinguishing feature of the constructed BOPs is that both the bond energy and the repulsive contribution to the cohesive energy comprise environmental dependencies. This is of primary importance for transferability of the potentials to environments significantly different from those of ideal structures for which most of the fitting is done. The testing of the potentials, summarised in this paper, demonstrates excellent transferability and thus the constructed BOPs are eminently suitable for atomistic studies of extended defects in the cores of which the local atomic environment is very different from that of ideal lattice structures.

The ability of the BOPs to reveal those aspects of dislocation behaviour that determine important and often unexpected features of plastic deformation has been demonstrated in applications of the constructed BOPs. In the case of titanium the angular bonding between the first nearest neighbours leads to a very high stacking fault energy on basal planes and thus spreading of screw dislocations to prism planes is favoured, leading to the strong preference for the prism slip. In molybdenum the screw dislocation core found using the BOP is non-degenerate, reflecting fully the symmetry of the bcc lattice. This is in full agreement with DFT-based calculations [155] but in contrast with many studies made using central-force potentials. The response of this dislocation core to the applied stresses, in particular the effect of shear stresses perpendicular to the Burgers vector, is strongly affected by the angular character of bonding. In iridium this feature of d-electron mediated bonding leads to the possible existence of two types of cores of screw dislocations. The first corresponding to the usual splitting into the Shockley partials and the second, which has never been found in any study of fcc metals, spread into two intersecting {1 1 1} planes. The latter

structure can serve as an intermediate configuration for the cross-slip that can then occur without the aid of thermal activation and can be unusually frequent even at low temperatures. This process offers a pathway for the anomalously high rates of dislocation multiplication that leads to rapid hardening which, in turn, is responsible for brittle fracture occurring after extensive plastic deformation, the phenomenon not observed in any other fcc metal. This demonstrates how strong angular character of bonding can lead to unusual mechanical behaviour. Finally, in the $L1_0$ TiAl the calculations show that cores of ordinary screw dislocations are always non-planar, again in full agreement with DFT-based calculations [176], and explain the asymmetry of glide of superdislocations. Both these features relate directly to the angular character of bonding that controls the energies of stacking fault-like defects which in turn control the core properties and thus all the aspects of the dislocation glide.

Nevertheless, despite the successes of these atom-based BOPs in modelling the mechanical properties of metals, their range of applicability is limited to non-dynamic simulations. This is due to non-negligible errors in the Hellmann–Feynman forces that have resulted from coarse graining the electronic structure in terms of a finite number of moments of the density of states. As is well known for metals, interactions in real space can be very long ranged and oscillatory, especially whenever Fermi surface nesting occurs in reciprocal space. The ensuing errors in the BOP density matrix or bond order imply corresponding errors in the Hellmann–Feynman force that may vary from configuration to configuration and thus from time step to time step in a molecular dynamics (MD) calculation. Owing to these errors, which result from the fact that the BOP Hellmann–Feynman force does not equal the numerical derivative of the BOP bond energy [43], equations of motions may not be solved with precision sufficient for the conservation of energy which is the first integral of equations of motion. Thus, the total energy may not to be conserved within molecular dynamics (MD) simulations. This problem is currently being addressed by deriving *analytic* atom-based BOPs for metals that would complement the analytic bond-based BOPs for semiconductors that are discussed in the following paper [61]. The corresponding analytic BOP forces would correspond to the numerical derivative of the analytic BOP energy, so that the total energy in any MD simulation would be conserved. The future challenge would then be to marry these analytic potentials for the unsaturated covalent bonds in metals with those for the saturated bonds in semiconductors so that technologically important alloys and compounds comprising elemental metals and semiconductors may be modelled.

Acknowledgements

Appendix A. Averaged scalar Lanczos algorithm

The averaged scalar Lanczos algorithm [55] was developed in a general form to derive the atom-based many-atom expansion of the inter-site Green's function that removes the

problems of orbital symmetry and violation of on-site–inter-site equivalence [39]. Here we illustrate the equivalence without introducing the auxiliary vector space which was used in [39].

We start from a list of vectors,

$$\mathbf{U}_0 \equiv (\mathbf{u}_0^{\alpha_1}, \mathbf{u}_0^{\alpha_2}, \ldots) \tag{A1}$$

where each vector represents an atomic orbital labelled by $\alpha_1, \alpha_2, \ldots$ We assume that the atomic orbitals are orthonormal, namely $(\mathbf{u}_0^{\alpha})^* \cdot \mathbf{u}_0^{\beta} = \delta_{\alpha,\beta}$. The Hamiltonian may act on this list as $\mathbf{HU}_0 = (\mathbf{Hu}_0^{\alpha_1}, \mathbf{Hu}_0^{\alpha_2}, \ldots)$. Following the recurrence rule,

$$\mathbf{HU}_n = \mathbf{U}_{n-1}b_n + \mathbf{U}_n a_n + \mathbf{U}_{n+1}b_{n+1} \tag{A2}$$

where a_n and b_n are scalar coefficients, the Lanczos recursion procedure [55] can be applied starting with $\mathbf{U}_0$ and $b_0 = 0$, requiring the orthonormality condition for the $\mathbf{U}$ vectors as

$$\{\mathbf{U}_m, \mathbf{U}_n\}_\Lambda = \delta_{m,n} \tag{A3}$$

Now we define the scalar product between the $\mathbf{U}$ vectors $\{\mathbf{U}_m, \mathbf{U}_n\}_\Lambda$ in a generalised form by

$$\{\mathbf{U}_m, \mathbf{U}_n\}_\Lambda \equiv \sum_{\alpha,\beta} (\mathbf{u}_m^{\alpha})^* \cdot \mathbf{u}_n^{\beta} \Lambda_{\alpha,\beta} \tag{A4}$$

with $\Lambda_{\alpha,\beta}$ being any such matrix that Eq. (A3) satisfies the well-known axioms of inner product. (For example, we may take $\Lambda_{\alpha,\beta} = (\mathbf{e}_\alpha)^* \cdot \mathbf{e}_\beta$, where $\{\mathbf{e}_{\alpha_1}, \mathbf{e}_{\alpha_2}, \ldots\}$ is an arbitrary set of complex vectors.)

The first few recursion coefficients may be written explicitly as

$$a_0 = \{\mathbf{U}_0, \mathbf{HU}_0\}_\Lambda = \mu_1 \tag{A5}$$

$$b_1^2 = \{\mathbf{U}_0, (\mathbf{H} - a_0\mathbf{I})^2\mathbf{U}_0\}_\Lambda = \mu_2 - \mu_1^2 \tag{A6}$$

$$a_1 = b_1^{-2}\{\mathbf{U}_0, \mathbf{H}(\mathbf{H} - a_0\mathbf{I})^2\mathbf{U}_0\}_\Lambda = \frac{\mu_3 - 2\mu_1\mu_2 + \mu_1^3}{\mu_2 - \mu_1^2} \tag{A7}$$

where the moments are given by

$$\mu_p = \{\mathbf{U}_0, \mathbf{H}^p\mathbf{U}_0\}_\Lambda = \sum_{\alpha,\beta} (\mathbf{u}_0^{\alpha})^* \cdot \mathbf{H}^p\mathbf{u}_0^{\beta} \Lambda_{\alpha,\beta} = \sum_{\alpha,\beta} \langle\alpha|\widehat{H}^p|\beta\rangle \Lambda_{\alpha,\beta} \tag{A8}$$

This gives an averaged moment when Λ is chosen to be a diagonal matrix. In particular, the choice $\Lambda_{I\mu,I\mu} = 1/d$ where the μ are the d-fold degenerate orbitals on atom I, and all the other elements zero gives the average moments on atom I. This is the choice for our atom-based bond-order potential.

The Green's functions along the Lanczos recursion chain are defined by

$$G_{nm}(z) = \{\mathbf{U}_n, (z\mathbf{I} - \mathbf{H})^{-1}\mathbf{U}_m\}_\Lambda \tag{A9}$$

The first diagonal Green's function may be written as

$$G_{00}(z) = \sum_{I\mu,J\nu} G_{I\mu,J\nu}(z) \Lambda_{I\mu,J\nu} \tag{A10}$$

and represented by a continued fraction, Eq. (5). This enables us to find the derivative of the generalised many-atom expansion of the inter-site Green's function,

$$G_{I\mu,Jv} = \frac{\partial G_{00}}{\partial \Lambda_{I\mu,Jv}} \tag{A11}$$

that is relevant for the case of multi-orbital atoms.

Appendix B. Truncators for inter-site Green's function

In practice Lanczos recursion chain is calculated only to some given level L, so that the many-atom expansion of the inter-site Green's function, Eqs. (21)–(28), namely

$$G_{I\mu,Jv} = \sum_{n=0}^{\infty} G_{0n}G_{n0}\delta a_n^{I\mu,Jv} + \sum_{n=1}^{\infty} 2G_{0(n-1)}G_{n0}\delta b_n^{I\mu,Jv} \tag{B1}$$

has to be approximated using a finite number of exact recursion coefficients up to a_{L-1} and b_{L-1}, and exact differential coefficients $\delta a_{L-1}^{I\mu,Jv}$ and $\delta b_{L-1}^{I\mu,Jv}$. As mentioned in the main text, the semi-infinite Lanczos recursion chain and G_{n0} for metallic systems may be approximated by setting $a_n = a_\infty$ and $b_n = b_\infty$ for $n \geqslant L$. A corresponding approximation for the many-atom expansion, Eq. (B1), should be made consistently in such a way that the equivalence of the on-site and inter-site expressions for the covalent bond energy is guaranteed. It follows from the matrix identity Eq. (17) that this equivalence is determined by the sum rule,

$$(z - H_{I\mu,I\mu})d^{-1}\sum_\mu G_{I\mu,I\mu}(z) = 1 + d^{-1}\sum_\mu \sum_{J(\neq I)v} H_{Jv,I\mu}G_{I\mu,Jv}(z) \tag{B2}$$

where μ under the summation symbol runs over d-fold degenerate orbitals of the same atomic energy level $H_{I\mu,I\mu}$ on atom I. This sum rule will not be fulfilled if we simply truncate the series in Eq. (B1) after the last exact differential coefficients (i.e. $\delta a_{L-2}^{I\mu,Jv}$ and $\delta b_{L-1}^{I\mu,Jv}$). Instead, a pair of additional coefficients, the so-called truncators,

$$\delta a_{L-1}^{I\mu,Jv} = \left(\frac{b_\infty^2 - b_{L-1}^2}{b_{L-1}}\right)o_{L-1,L-2}^{I\mu,Jv} \tag{B3}$$

$$\delta b_L^{I\mu,Jv} = \frac{1}{2}\left(\frac{b_\infty(a_\infty - a_{L-1})}{b_{L-1}}\right)o_{L-1,L-2}^{I\mu,Jv} \tag{B4}$$

can be constructed and used to guarantee the sum rule. Here we have introduced

$$o_{m,n}^{I\mu,Jv} = \langle I\mu|P_m(\widehat{H})P_n(\widehat{H})|Jv\rangle \tag{B5}$$

where the polynomials of x, $P_n(x)$, are defined by

$$b_{n+1}P_{n+1}(x) = (x - a_n)P_n(x) - b_nP_{n-1}(x) \tag{B6}$$

with $P_{-1}(x) = 0$ and $P_0(x) = 1$.

In order to illustrate the role of the truncators, Eqs. (B3) and (B4), we first derive a useful formula. It follows from the recursive relation for the Green's function along the Lanczos recursion chain, namely

$$(z - a_n)G_{n0}(z) = b_nG_{(n-1)0}(z) + b_{n+1}G_{(n+1)0}(z) + \delta_{n,0} \tag{B7}$$

with $b_0 \equiv 0$, that for any $N \geqslant 1$

$$b_1 G_{10} = \sum_{n=0}^{N-1} (b_{n+1}^2 - b_n^2) G_{n0} G_{n0} + \sum_{n=1}^{N} b_n (a_n - a_{n-1}) G_{n0} G_{(n-1)0} + \Delta_N \tag{B8}$$

where $\Delta_N = b_N b_{N+1} G_{(N-1)0} G_{(N+1)0} - b_N^2 G_{N0} G_{N0}$. If we make the approximation that $a_n = a_\infty$ and $b_n = b_\infty$ for $n \geqslant L$, then Eq. (B8) with $N = L$ gives the key formula

$$b_1 G_{10} = \sum_{n=0}^{L-1} (b_{n+1}^2 - b_n^2) G_{n0} G_{n0} + \sum_{n=1}^{L} b_n (a_n - a_{n-1}) G_{n0} G_{(n-1)0} \tag{B9}$$

since $\Delta_L = b_\infty^2 G_{(L-1)0} G_{(L+1)0} - b_\infty^2 G_{L0} G_{L0} = 0$. This can be confirmed by using the relations , $b_\infty G_{L0} / G_{(L-1)0} = T$ and $b_\infty G_{(L+1)0} / G_{L0} = T$, which are the consequence of Eq. (B7) with T denoting the square root terminator Eq. (8).

Recalling that G_{00} is defined as an average Green's function about atom I, namely

$$G_{00}(z) = d^{-1} \sum_\mu G_{I\mu, I\mu}(z) \tag{B10}$$

and using Eq. (B7) with $n = 0$, the sum rule (B2) with formula (B9) gives

$$d^{-1} \sum_\mu \sum_{J(\neq I)\nu} H_{J\nu, I\mu} G_{I\mu, J\nu}(z) = \sum_{n=0}^{L-1} (b_{n+1}^2 - b_n^2) G_{n0} G_{n0}$$
$$+ \sum_{n=1}^{L} b_n (a_n - a_{n-1}) G_{n0} G_{(n-1)0}. \tag{B11}$$

Substituting the many-atom expansion Eq. (B1) into Eq. (B11), we identify

$$d^{-1} \sum_\mu \sum_{J(\neq I)\nu} H_{J\nu, I\mu} \delta a_n^{I\mu, J\nu} = b_{n+1}^2 - b_n^2 \tag{B12}$$

and

$$d^{-1} \sum_\mu \sum_{J(\neq I)\nu} H_{J\nu, I\mu} \delta b_n^{I\mu, J\nu} = \frac{1}{2} b_n (a_n - a_{n-1}). \tag{B13}$$

Therefore, the sum rule (B2) implies that $\delta a_{L-1}^{I\mu, J\nu}$ and $\delta b_L^{I\mu, J\nu}$ need to be constructed in such a way that they satisfy Eqs. (B12) and (B13) if the truncated many-atom expansion

$$G_{I\mu, J\nu} = \sum_{n=0}^{L-1} G_{0n} G_{n0} \delta a_n^{I\mu, J\nu} + \sum_{n=1}^{L} 2 G_{0(n-1)} G_{n0} \delta b_n^{I\mu, J\nu} \tag{B14}$$

is to satisfy the sum rule. Particular forms of the truncators, (B3) and (B4), are designed using the property

$$d^{-1} \sum_\mu \sum_{J(\neq I)\nu} H_{J\nu, I\mu} o_{n,n-1}^{I\mu, J\nu} = b_n. \tag{B15}$$

Further properties of o-matrices are described in Refs. [42,43].

References

[1] Ernst F, Rühle M. Curr Opin Solid State Mater Sci 1997;2:469.
[2] Smith DJ. Rep Prog Phys 1997;60:1513.
[3] Spence JCH. Mater Sci Eng R 1999;26:1.

[4] Pennycook SJ. In: Hawkes PW, editor. Advances in imaging and elect phys, vol. 123. San Diego: Academic Press; 2002. p. 173.
[5] Tersoff J, Vanderbilt D, Vitek V, editors. Atomic scale calculations in materials science, vol. 141. Pittsburgh: Materials Research Society; 1989.
[6] Daw MS, Schlüter MA, editors. Atomic scale calculations in materials science, vol. 193. Pittsburgh: Materials Research Society; 1990.
[7] Broughton J, Bristowe P, Newsam J, editors. Materials theory and modelling, vol. 291. Pittsburgh: Materials Research Society; 1993.
[8] Raabe D. Computational materials science: the simulation of materials, microstructures and properties. New York: Wiley VCH; 1998.
[9] Bulatov VV, de la Rubia TD, Phillips R, Kaxiras E, Ghoniem N, editors. Multiscale modelling of materials, vol. 538. Pittsburgh: Materials Research Society; 1999.
[10] Yip S, editor. Handbook of materials modelling. New York: Springer; 2005.
[11] Pettifor DG, Cottrell AH, editors. Electron theory in alloy design. London: The Institute of Materials; 1992.
[12] Finnis MW. Interatomic forces in condensed matter. Oxford: Oxford University Press; 2003.
[13] Finnis M. Prog Mater Sci 2004;49:1.
[14] Pettifor DG. Phys Educ 1997;32:164.
[15] Voter AF, editor. MRS Bulletin 1996;21(2).
[16] Daw MS, Baskes MI. Phys Rev B 1984;29:6443.
[17] Daw MS, Foiles SM, Baskes MI. Mater Sci Rep 1993;9:251.
[18] Foiles SM. MRS Bull 1996;21:24.
[19] Finnis MW, Sinclair JE. Philos Mag A 1984;50:45.
[20] Ackland GJ, Tichy G, Vitek V, Finnis MW. Philos Mag A 1987;56:735.
[21] Ackland GJ, Finnis MW, Vitek V. J Phys F: Metal Phys 1988;18:L153.
[22] Friedel J. In: Ziman JM, editor. The physics of metals. Cambridge: Cambridge University Press; 1969. p. 340.
[23] Pettifor DG. Bonding and structure of molecules and solids. Oxford: Oxford University Press; 1995.
[24] Woodward C, MacLaren JM, Rao SI. J Mater Res 1992;7:1735.
[25] Nguyen-Manh D, Bratkovsky AM, Pettifor DG. Phil Trans Roy Soc London A 1995;351:529.
[26] Yoo MH, Zou J, Fu CL. Mater Sci Eng A 1995;193:14.
[27] Nguyen-Manh D, Pettifor DG. Intermetallics 1999;7:1095.
[28] Baskes MI. Phys Rev B 1992;46:2727.
[29] Baskes MI, Johnson RA. Modell Simul Mater Sci Eng 1994;2:147.
[30] Lee BJ, Baskes MI, Kim H, Cho YK. Phys Rev B 2001;64:184102.
[31] Lee BJ, Shim JH, Baskes MI. Phys Rev B 2003;68:144112.
[32] Moriarty JA. Phys Rev B 1990;42:1609.
[33] Moriarty JA. Phys Rev B 1994;49:12431.
[34] AlLehyani I, Widom M, Wang Y, Moghadam N, Stocks GM, Moriarty JA. Phys Rev B 2001;64:075109.
[35] Coulson CA. Proc Roy Soc London A 1939;169:413.
[36] Pettifor DG. Phys Rev Lett 1989;63:2480.
[37] Pettifor DG. In: Nieminen RM, Puska J, Manninen M, editors. Many atom interactions in solids, vol. 48. Berlin: Springer; 1990. p. 64.
[38] Aoki M, Gumbsch P, Pettifor DG. In: Terakura T, Akai H, editors. Interatomic potentials and structural stability, vol. 114. Berlin: Springer; 1993. p. 23.
[39] Aoki M. Phys Rev Lett 1993;71:3842.
[40] Aoki M, Pettifor DG. Mat Sci Eng A 1994;176:19.
[41] Aoki M, Pettifor DG. In: Oppeneer PM, Kübler J, editors. Physics of transition metals. Singapore: World Scientific; 1993. p. 299.
[42] Horsfield AP, Bratkovsky AM, Pettifor DG, Aoki M. Phys Rev B 1996;53:1656.
[43] Horsfield AP, Bratkovsky AM, Fearn M, Pettifor DG, Aoki M. Phys Rev B 1996;53:12694.
[44] Horsfield AP, Bratkovsky AM. Phys Rev B 1996;53:15381.
[45] Bowler DR, Aoki M, Goringe CM, Horsfield AP, Pettifor DG. Modell Simul Mater Sci Eng 1997;5:199.
[46] Hellmann H. Einführung in die Quantenchemie. Leipzig: Franz Deuticke; 1937.
[47] Feynman RP. Phys Rev 1939;56:340.
[48] Girshick A, Bratkovsky AM, Pettifor DG, Vitek V. Philos Mag A 1998;77:981.
[49] Mrovec M, Nguyen-Manh D, Pettifor DG, Vitek V. Phys Rev B 2004;69:094115.
[50] Cawkwell MJ, Nguyen-Manh D, Woodward C, Pettifor DG, Vitek V. Science 2005;309:1059.

[51] Cawkwell MJ, Nguyen-Manh D, Pettifor DG, Vitek V. Phys Rev B 2006;73:064104.

[52] Znam S, Nguyen-Manh D, Pettifor DG, Vitek V. Philos Mag 2003;83:415.

[53] Cawkwell MJ, Mrovec M, Nguyen-Manh D, Pettifor DG, Vitek V. In: Mills MJ, Clemens H, Fu C-L, Inui H, editors. Integrative and interdisciplinary aspects of intermetallics, vol. 842. Pittsburgh: Materials Research Society; 2005. p. S2.8.1.

[54] Finnis MW. Prog Mater Sci 2006; this volume, doi:10.1016/j.pmatsci.2006.10.004.

[55] Lanczos CJ. Res Natl Bur Stand 1950;45:225.

[56] Beer N, Pettifor DG. In: Phariseau P, Temmerman W, editors. Structure and phase stability of alloys. New York: Plenum Press; 1984.

[57] Slater JC, Koster GF. Phys Rev 1954;94:1498.

[58] Glanville S, Paxton AT, Finnis MW. J Phys F: Metal Phys 1988;18:693.

[59] Pettifor DG, Aoki M. Phil Trans Roy Soc London A 1991;334:439.

[60] Turchi P, Ducastelle F. In: Pettifor DG, Weaire DL, editors. The recursion method and its applications. Berlin: Springer; 1985. p. 104.

[61] Drautz R, Zhou XW, Murdick DA, Gillespie B, Wadley HNG, Pettifor DG. Prog Mater Sci 2006; this volume, doi:10.1016/j.pmatsci.2006.10.013.

[62] Ozaki T. Phys Rev B 1999;59:16061.

[63] Ozaki T, Aoki M, Pettifor DG. Phys Rev B 2000;61:7972.

[64] Goodwin L, Skinner AJ, Pettifor DG. Europhys Lett 1989;9:701.

[65] Nguyen-Manh D, Vitek V, Horsfield AP. Prog Mater Sci 2006; this volume, doi:10.1016/j.pmatsci.2006.10.010.

[66] Haas H, Wang CZ, Fähnle M, Elsässer C, Ho KM. Phys Rev B 1998;57:1461.

[67] Nguyen-Manh D, Pettifor DG, Vitek V. Phys Rev Lett 2000;85:4136.

[68] Nguyen-Manh D, Pettifor DG, Znam S, Vitek V. In: Turchi PEA, Gonis A, Colombo L, editors. Tight-binding approach to computational materials science, vol. 491. Pittsburgh: Materials Research Society; 1998. p. 353.

[69] Pettifor DG. In: Cahn RW, Haasen P, editors. Physical metallurgy. Amsterdam: Elsevier; 1983. p. 147.

[70] Andersen OK. Phys Rev B 1975;12:3060.

[71] Harrison WA. Electronic structure and properties of solids. San Francisco: Freeman; 1980.

[72] Rose JH, Smith JR, Ferrante J. Phys Rev B 1983;28:1835.

[73] Rose JH, Smith JR, Guinea F, Ferrante J. Phys Rev B 1984;29:2963.

[74] Rose JH, Shore HB. Phys Rev B 1991;43:11605.

[75] Nguyen-Manh D, Pettifor DG, Shao G, Miodownik AP, Pasturel A. Philos Mag A 1996;74:1385.

[76] Methfessel M. Phys Rev B 1988;38:1537.

[77] Andersen OK, Jepsen O, Sob M. In: Yussouff M, editor. Electronic band structure and its applications. New York: Springer; 1987. p. 1.

[78] Paidar V, Wang LG, Sob M, Vitek V. Modell Simul Mater Sci Eng 1999;7:369.

[79] Madsen GKH, Blaha P, Schwartz K, Sjöstedt E, Nordström L. Phys Rev B 2001;64:195134.

[80] Blaha P, Schwartz K, Madsen GKH, Kvasnicka D, Luitz J. WIEN2k, An augmented plane-wave + local orbitals program for calculating crystal properties. Austria: Karlheinz Schwarz, Technische Universität Wien; 2001.

[81] Mrovec M, Vitek V, Nguyen-Manh D, Pettifor DG, Wang LG, Sob M. In: Bulatov V, de la Rubia TD, Phillips R, Kaxiras E, Ghoniem N, editors. Multiscale modelling of materials, vol. 538. Pittsburgh: Materials Research Society; 1999. p. 529.

[82] Meyer B, Fähnle M. Phys Rev B 1997;56:13595.

[83] Xu W, Moriarty JA. Phys Rev B 1996;54:6941.

[84] Soderlind P, Yang LH, Moriarty JA, Wills JM. Phys Rev B 2000;61:2579.

[85] Kunc K. Electronic structure dynamics and quantum structure properties of condensed matter. New York: Plenum Press; 1985.

[86] Haasen P, Hieber H, Mordike BL. Z Metall 1965;56:832.

[87] Brookes CA, Greenwood JH, Routbort JL. J Inst Metals 1970;98:27.

[88] Hecker SS, Rohr DL, Stein DF. Metall Trans A 1978;9:481.

[89] Hunt LB. Platinum Metals Rev 1987;31:32.

[90] Panfilov P, Yermakov A. J Mater Sci 2004;39:4543.

[91] MacFarlane RE, Rayne JA, Jones CT. Phys Lett 1966;20:234.

[92] Maurer D, Heichele R, Lingg N, Muller V, Rieder KH. Phys Stat Sol A 1997;160:403.

[93] Heid R, Bohnen KP, Felix K, Ho KM, Reichardt W. J Phys: Condens Matter 1998;10:7967.
[94] Kittel C. Introduction to solid state physics. New York: John Wiley; 1986.
[95] Schwarz K, Blaha P. Comput Mater Sci 2003;28:259.
[96] Balk TJ, Hemker KJ. Mater Sci Eng A 2001;309:108.
[97] Gornostyrev YN, Katsnelson MI, Medvedeva NI, Mryasov ON, Freeman AJ, Trefilov AV. Phys Rev B 2000;62:7802.
[98] Korzhavyi PA, Abrikosov IA, Johansson B, Ruban AV, Skriver HL. Phys Rev B 1999;59:11693.
[99] Jacucci G, Taylor R, Tenenbaum A, Van Doan N. J Phys F Metal Phys 1981;11:793.
[100] Kim YW. Intermetallics 1998;6:623.
[101] Dimiduk DM. Mater Sci Eng A 1999;263:281.
[102] Yamaguchi M, Inui H, Ito K. Acta Mater 2000;48:307.
[103] Loria EA. Intermetallics 2001;9:997.
[104] Yamaguchi M, Inui H, Yokoshima S, Kishida K, Johnson DR. Mater Sci Eng A 1996;213:25.
[105] Inui H, Matsumuro M, Wu DH, Yamaguchi M. Philos Mag A 1997;75:395.
[106] Inui H, Chikugo K, Nomura K, Yamaguchi M. Mater Sci Eng A 2002;329:377.
[107] Farkas D. Modell Simul Mater Sci Eng 1994;2:975.
[108] Simmons JP, Rao SI, Dimiduk DM. Philos Mag A 1997;75:1299.
[109] Tanaka K, Ichitsubo T, Inui H, Yamaguchi M, Koiwa M. Philos Mag Lett 1996;73:71.
[110] Andersen OK, Jepsen O. Phys Rev Lett 1984;53:2571.
[111] Andersen OK, Jepsen O, Glötzel D. In: Bassani F, Fumi F, Tosi MP, editors. Highlights of condensed matter theory. Amsterdam: North Holland; 1985. p. 59.
[112] Nakamura H, NguyenManh D, Pettifor DG. J Alloys Comp 2000;306:113.
[113] Pettifor DG, Podloucky R. Phys Rev Lett 1984;53:1080.
[114] Pearson WB. Handbook of lattice spacings and structures of metals and alloys. Oxford: Pergamon Press; 1967.
[115] Znam S, Nguyen-Manh D, Pettifor DG, Vitek V. In: Meike A, Gonis A, Turchi PEA, Rajan K, editors. Properties of complex inorganic solids, vol. 2. Dordrecht, The Netherlands: Kluwer Academic/Plenum; 2000. p. 479.
[116] Tanaka K, Okamoto K, Inui H, Minonishi Y, Yamaguchi M, Koiwa M. Philos Mag A 1996;73:1475.
[117] Fu CL, Zou J, Yoo MH. Scripta Metall Mater 1995;33:885.
[118] Hirth JP, Lothe J. Theory of dislocations. New York: Wiley-Interscience; 1982.
[119] Duesbery MS. In: Nabarro FRN, editor. Dislocations in solids, vol. 8. Amsterdam: Elsevier; 1989. p. 67.
[120] Duesbery MS, Richardson GY. CRC Crit Rev Solid State Mater Sci 1991;17:1.
[121] Vitek V. Prog Mater Sci 1992;36:1.
[122] Caillard D, Couret A. In: Nabarro FRN, Duesbery MS, editors. Dislocations in solids, vol. 10. Amsterdam: Elsevier; 1996. p. 69.
[123] Takeuchi S. Radiat Eff Def Solids 1999;148:333.
[124] Hirth JP. Acta Mater 2000;48:93.
[125] Cai W, Bulatov VV, Chang J, Li J, Yip S. In: Nabarro FRN, Hirth JP, editors. Dislocations in solids, vol. 12. Amsterdam: Elsevier; 2004. p. 1.
[126] Hemker KJ, Viguier B, Mills MJ. Mater Sci Eng A 1993;164:391.
[127] Mills MJ, Daw MS, Foiles SM. Ultramicroscopy 1994;56:79.
[128] Inkson BJ, Humphreys CJ. Philos Mag Lett 1995;71:307.
[129] Sigle W. Philos Mag A 1999;79:1009.
[130] Balk TJ, Hemker KJ. Philos Mag A 2001;81:1507.
[131] Kamimura Y, Edagawa K, Noda M, Suzuki K, Takeuchi S. Mater Sci Eng A 2004;387–389:29.
[132] Vitek V. Philos Mag A 1968;18:773.
[133] Christian JW, Vitek V. Rep Prog Phys 1970;33:307.
[134] Schoeck G. Philos Mag A 1994;69:1085.
[135] Mryasov ON, Gornostyrev YN, Freeman AJ. Phys Rev B 1998;58:11927.
[136] Woodward C, Rao SI. Phys Rev Lett 2002;8821:6402.
[137] Girshick A, Pettifor DG, Vitek V. Philos Mag A 1998;77:999.
[138] Legrand PB. In: Veyssiere P, Kubin LP, Castaing J, editors. Dislocations 1984. Paris: Editions CNRS; 1984. p. 73.
[139] Legrand PB. Philos Mag A 1985;52:83.
[140] Churchman AT. Met Trans AIME 1954;218:262.

[141] Bacon DJ, Vitek V. Metall Mater Trans A 2002;33:721.
[142] Ackland GJ. Philos Mag A 1992;66:917.
[143] Vitek V, Mrovec M, Bassani JL. Mater Sci Eng A 2004;365:31.
[144] Vitek V, Mrovec A, Gröger R, Bassani JL, Racherla V, Yin L. Mater Sci Eng A 2004;387–89:138.
[145] Vitek V. Philos Mag 2004;84:415.
[146] Gröger R, Vitek V. Mater Sci Forum 2005;482:123.
[147] Christian JW. In: Leslie WC, editor. Second int conference on the strength of metals and alloys. Metals Park, Ohio: ASM; 1970. p. 31.
[148] Vitek V. Cryst Latt Def 1974;5:1.
[149] Kubin LP. Rev Deform Behav Materials 1982;4:181.
[150] Christian JW. Metall Trans A 1983;14:1237.
[151] Frederiksen SL, Jacobsen KW. Philos Mag 2003;83:365.
[152] Hirsch PB. Proc 5th int conf crystallography. Cambridge University; 1960. p. 139.
[153] Suzuki H. In: Rosenfield AR, Hahn GT, Bement AL, Jaffee RI, editors. Dislocation dynamics. New York: McGraw-Hill; 1968. p. 679.
[154] Duesbery MS, Vitek V, Cserti J. In: Humphreys CJ, editor. Understanding materials: a Festschrift for Sir Peter Hirsch. London: The Institute of Materials; 2002. p. 165.
[155] Woodward C, Rao SI. Philos Mag A 2001;81:1305.
[156] Basinski ZS, Duesbery MS, Taylor R. Can J Phys 1971;49:2160.
[157] Basinski ZS, Duesbery MS, Murthy GS. Acta Metall 1981;29:801.
[158] Duesbery MS. Proc Roy Soc London A 1984;392:145.
[159] Duesbery MS. Proc Roy Soc London A 1984;392:175.
[160] Duesbery MS, Vitek V. Acta Mater 1998;46:1481.
[161] Seeger A. J Phys IV 1995;5:45.
[162] Hollang L, Hommel M, Seeger A. Phys Stat Sol (a) 1997;160:329.
[163] Ito K, Vitek V. Philos Mag A 2001;81:1387.
[164] Jeffcoat PJ, Mordike BL, Rogausch KD. Philos Mag 1976;34:583.
[165] Escaig B. J Phys France 1968;29:225.
[166] Cawkwell MJ, Woodward C, Nguyen-Manh D, Pettifor DG, Vitek V. Acta Mater, in press.
[167] Panfilov P, Yermakov A, Dmitriev V, Timofeev N. Platinum Metals Rev 1991;35:196.
[168] Porizek R, Znam S, Nguyen-Manh D, Vitek V, Pettifor DG. In: George EP, Inui H, Mills MJ, Eggeler G, editors. Defect properties and related phenomena in intermetallic alloys, vol. 753. Pittsburgh: Materials Research Society; 2003. p. BB4.3.1.
[169] Sriram S, Vasudevan VK, Dimiduk D. In: Horton JA, Baker I, Hanada S, Noebe RD, Schwartz DS, editors. High-temperature ordered intermetallic alloys VI, vol. 364. Pittsburgh: Materials Research Society; 1999. p. 647.
[170] Song Y, Tang SP, Xu JH, Mryasov ON, Freeman AJ, Woodward C, et al. Philos Mag B 1994;70:987.
[171] Zou J, Fu CL, Yoo MH. Intermetallics 1995;3:265.
[172] Nguyen-Manh D, Pettifor DG. In: Kim YW, editor. Gamma titanium aluminides. Pittsburgh: TMS; 1999. p. 175.
[173] Vitek V, Ito K, Siegl R, Znam S. Mater Sci Eng A 1997;240:752.
[174] Ehmann J, Fähnle M. Philos Mag A 1998;77:701.
[175] Paidar V, Vitek V. In: Westbrook JH, Fleisher RL, editors. Intermetallic compouds: principles and practice, vol. 3. New York: John Wiley; 2002. p. 437.
[176] Woodward C, Rao SI. Philos Mag 2004;84:401.
[177] Inui H, Yamaguchi M. Electron Microscopy 1997;32:144.
[178] Veyssiere P, Chiu Y-L, Gregori F. In: George EP, Inui H, Mills MJ, Eggeler G, editors. Defect properties and related phenomena in intermetallic alloys, vol. 753. Pittsburgh: Materials Research Society; 2003. p. BB4.1.
[179] Kishida K, Inui H, Yamaguchi M. Philos Mag A 1998;78:1.
[180] Kishida K, Inui H, Yamaguchi M. Intermetallics 1999;7:1131.
[181] Kim M, Nomura M, Vitek V, Pope D. In: George EP, Mills MJ, Yamaguchi M, editors. High-temperature ordered intermetallic alloys VIII, vol. 552. Pittsburgh: Materials Research Society; 1999. p. KK3.1.1.
[182] Chen Y, Pope DP, Vitek V. In: George EP, Inui H, Mills MJ, Eggeler G, editors. Defect properties and related phenomena in intermetallic alloys, vol. 753. Pittsburgh: Materials Research Society; 2003. p. BB3.10.1.
[183] Katzarov IH, Cawkwell MJ, Paxton AT, Finnis MW. Philos Mag, to be published.